CONSTRUCTION OF AN ULTRA–THIN CYLINDRICAL DRIFT CHAMBER FOR MEASUREMENT OF THE RARE DECAY $K^+ \to \pi^+ \nu\overline{\nu}$

By

Vighen Pacradouni

B.Sc., McGill University, 1989

B.Eng., McGill University, 1991

A THESIS SUBMITTED IN PARTIAL FULFILLMENT OF

THE REQUIREMENTS FOR THE DEGREE OF

MASTER OF SCIENCE

in

THE FACULTY OF GRADUATE STUDIES

DEPARTMENT OF PHYSICS

We accept this thesis as conforming

to the required standard

THE UNIVERSITY OF BRITISH COLUMBIA

September 1993

In presenting this thesis in partial fulfilment of the requirements for an advanced degree at the University of British Columbia, I agree that the Library shall make it freely available for reference and study. I further agree that permission for extensive copying of this thesis for scholarly purposes may be granted by the head of my department or by his or her representatives. It is understood that copying or publication of this thesis for financial gain shall not be allowed without my written permission.

Department of Physics
The University of British Columbia
2075 Wesbrook Place
Vancouver, Canada
V6T 1W5

Date: September 9, 1993

Abstract

The branching ratio for the decay $K^+ \rightarrow \pi^+ \nu\bar{\nu}$ has been measured at Brookhaven National Laboratory by the E787 collaboration to be 5.2×10^{-9}. The best QCD calculations give a prediction of $(.6 \rightarrow 6) \times 10^{-10}$. The theoretical equations for this calculation as well as the previous experiment are reviewed. The experiment is in the midst of a major upgrade resulting in a new beam line and a modified detector. The ultra–thin cylindrical drift–chamber with helical cathode strips for measurement of the axial coordinate of the charged particle track is described. A design for charge pre–amplifiers to instrument the cathode strips is discussed. The desired gain was achieved for single amplifiers, however, the problem of ringing and cross–talk when mounted in close proximity remains.

Table of Contents

List of Tables

List of Figures

Chapter 1

Introduction

Experiment 787 at Brookhaven National Laboratory is a search for the second order weak decay, $K^+ \rightarrow \pi^+\nu\overline{\nu}$. The experiment is a BNL–Princeton–collaboration which has constructed, operates and maintains a detector optimized for the measurement of the above decay. The detector is located at BNL's Alternating Gradient Synchrotron facility.

The last experimental run was in 1991, and while no candidate events have been found to date, an upper limit for the branching ratio of $K^+ \rightarrow \pi^+\nu\overline{\nu}$ has been set at 5.2×10^{-9} at the 90% confidence level [1]. The collaboration is now in the midst of upgrading the detector. Part of this upgrade consists of replacing the current central tracking drift chamber with a new one having a lower mass and an improved momentum resolution. The new drift chamber, called the ultra–thin chamber (UTC) is the topic of this thesis.

Chapter 2 presents a cursory description of electroweak theory as it relates to $K^+ \rightarrow \pi^+\nu\overline{\nu}$. It also describes the significance of the decay mode in the Standard Model and the extraction of Standard Model parameters from a measurement of the $K^+ \rightarrow \pi^+\nu\overline{\nu}$ branching ratio. Chapter 3 describes the problems involved in the measurement of the decay and the general strategies and techniques used in overcoming these difficulties. Chapter 4 presents an overview of the entire E787 detector giving brief descriptions of its various components. Chapter 5 deals with the UTC itself. It provides a physical description, an explanation of its operation, the motivation behind its design, the results of studies of its momentum resolution, and finally the effects of an improved momentum resolution on the measurement of $K^+ \rightarrow \pi^+\nu\overline{\nu}$. The UTC uses cathode foil strip charge readouts to perform tracking in the axial direction, a feature not found in the existing drift chamber. Although the existing pre–amplifiers can be used for the sense wires they are certainly not optimal for the cathode strips. This is due to the electrical characteristics of the cathode strips as well as the time evolution of the charge that they collect. Chapter 6 provides a description of the existing anode amplifiers and presents a design for a charge amplifier to instrument the cathode strips.

Chapter 2

Theory

2.1 Role in Weak Theory

Kaon decays have historically played an important role in the development of the theory of weak interactions. In particular, a study of these phenomena contributed to the discovery of parity violation and to the prediction of the existence of the charmed quark. The process $K^+ \rightarrow \pi^+ \nu\overline{\nu}$, a rare decay, offers the possibility of being a hunting ground for new physics or a test of the higher order predictions of the Standard Model.

An attempt to develop a theory of a so-called weak interaction to describe the decay of long-lived states such as nuclear beta decay, kaon decay, and muon decay produced the V-A theory of Feynman and Gell-Mann [26]. This was a Lorentz covariant theory of charged current interactions. The name V-A is derived from the fact that the currents contain terms like $\overline{\psi}\gamma^\mu(1-\gamma^5)\psi$ where ψ,$\overline{\psi}$ are the Dirac spinors and their adjoints, and the γ^μ and $\gamma^\mu\gamma^5$ parts transform respectively as vectors and axial-vectors under parity transformations.

Although this theory accommodated parity violation, which had invalidated the Fermi theory, it nevertheless required different coupling constants to account for the differing rates of decay. In the context of quark theory, the nuclear beta decays and kaon decays corresponded to $(d \rightarrow u)$ and $(s \rightarrow u)$ transitions respectively. Cabibbo noticed that a lone universal constant would accurately describe transition rates in all three cases if one one were to treat the weak eigenstate, d', that is, the particle that participates in the weak interaction, as a rotated superposition of d and s [27]. Thus, the weak isospin doublet becomes:

$$\begin{pmatrix} u \\ d' \end{pmatrix} = \begin{pmatrix} u \\ d\cos\theta_c + s\sin\theta_c \end{pmatrix}$$

with $\theta_c \approx 13^o$.

Now, given the presence of charged current interactions one was led naturally to expect neutral currents as well. In the Cabibbo theory with its sole doublet, the neutral current consisted of the transitions $(u \rightarrow u)$ and $d' \rightarrow d')$. This yields a neutral current of:

$$J_{NC} = \overline{u}u + \overline{d'}d'$$

$$= \overline{u}u + \overline{d}d\cos^2\theta_c + \overline{s}s\sin^2\theta_c + (\overline{d}s + \overline{s}d)\cos\theta_c\sin\theta_c$$

clearly representing a non-zero, and non-suppressed amplitude for $(s \to d)$ transitions.

Decays such as these, involving flavour changing neutral currents, of which the decay $K^+ \to \pi^+\nu\overline{\nu}$ is an example, were searched for but either not found or else were found to be extremely suppressed compared to their charged current counterparts.

2.2 G.I.M Mechanism

In 1970, Glashow, Illiopoulos, and Maiani, suggested a mechanism, subsequently named the G.I.M mechanism, to account for the suppression of these flavour changing neutral currents [25]. They proposed the existence of a second doublet and thus extended the Cabibbo model to four quarks arranged in two orthogonal doublets:

$$\begin{pmatrix} u \\ d' \end{pmatrix} \begin{pmatrix} c \\ s' \end{pmatrix}$$

with the weak eigenstate down-like quarks related to the strong eigenstates by a rotation matrix, i.e. :

$$\begin{pmatrix} d' \\ s' \end{pmatrix} = \underbrace{\begin{pmatrix} \cos\theta_c & \sin\theta_c \\ -\sin\theta_c & \cos\theta_c \end{pmatrix}}_{M_c} \begin{pmatrix} d \\ s \end{pmatrix}$$

Now, the neutral current is composed of terms like:

$$\begin{aligned} J_{NC} &= \overline{u}u + \overline{c}c + \overline{d'}d' + \overline{s'}s' \\ &= \overline{u}u + \overline{c}c + \begin{pmatrix} \overline{d'} & \overline{s'} \end{pmatrix} \begin{pmatrix} d' \\ s' \end{pmatrix} \\ &= \overline{u}u + \overline{c}c + \begin{pmatrix} \overline{d} & \overline{s} \end{pmatrix} M_c^\dagger M_c \begin{pmatrix} d \\ s \end{pmatrix} \\ &= \overline{u}u + \overline{c}c + \overline{d}d + \overline{s}s \end{aligned}$$

so that the flavour-changing part of the neutral current vanishes due to the unitarity of the mixing matrix, and this remains true for an arbitrary number of generations with the appropriately dimensioned mixing matrix.

2.3 The CKM Matrix

In the present-day six quark model we have three doublets [31]:

$$\begin{pmatrix} u \\ d' \end{pmatrix} \quad \begin{pmatrix} c \\ s' \end{pmatrix} \quad \begin{pmatrix} t \\ b' \end{pmatrix}$$

with

$$\begin{pmatrix} d' \\ s' \\ b' \end{pmatrix} = \underbrace{\begin{pmatrix} V_{ud} & V_{us} & V_{ub} \\ V_{cd} & V_{cs} & V_{cb} \\ V_{td} & V_{ts} & V_{tb} \end{pmatrix}}_{M_c} \begin{pmatrix} d \\ s \\ b \end{pmatrix} \tag{2.1}$$

The matrix, M_c, is called the Cabibbo-Kobayashi-Maskawa (CKM) matrix. The neutral currents are:

$$\begin{aligned} J_{NC} &= \overline{u}u + \overline{c}c + \overline{t}t + \overline{d'}d' + \overline{s'}s' + \overline{b'}b' \\ &= \overline{u}u + \overline{c}c + \overline{t}t + \begin{pmatrix} \overline{d} & \overline{s} & \overline{b} \end{pmatrix} M_c^{\dagger} M_c \begin{pmatrix} d \\ s \\ b \end{pmatrix} \\ &= \overline{u}u + \overline{c}c + \overline{t}t + \overline{d}d + \overline{s}s + \overline{b}b \end{aligned}$$

so that, once again the flavour-changing component vanishes.

2.4 Theoretical Significance of the Decay $K^+ \to \pi^+ \nu \overline{\nu}$

We now consider the significance of the existence of the $K^+ \to \pi^+ \nu \overline{\nu}$ decay mode. Figure 2.1 shows the allowed decay $K^+ \to \pi^0 e^+ \nu$ which proceeds via a charged W^+ current with a branching ratio (BR) of 5%. Figure 2.2 shows the first order Feynman diagram for the $K^+ \to$

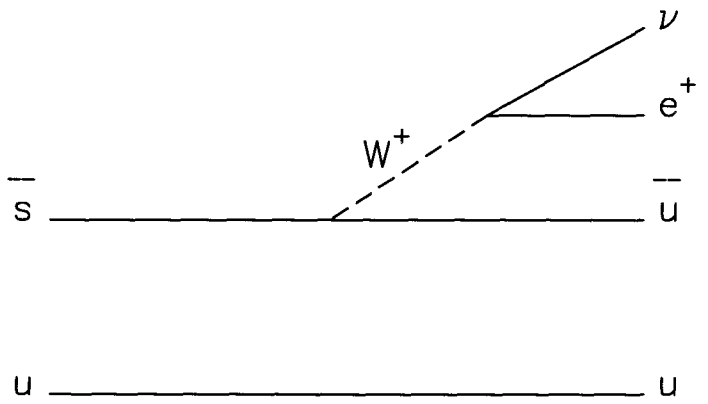

Figure 2.1: Feynman Diagram for $K^+ \to \pi^0 e^+ \nu$

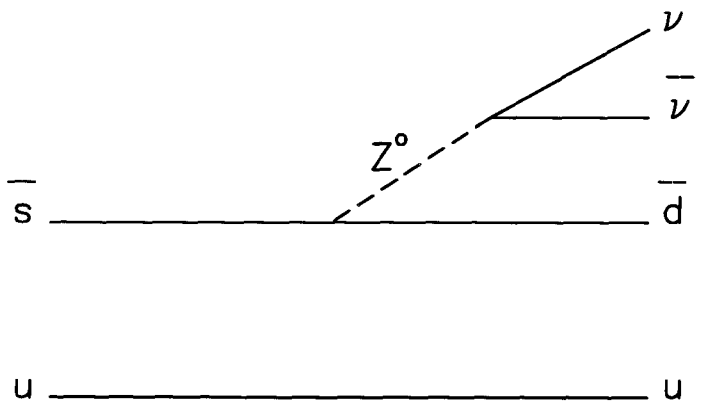

Figure 2.2: Feynman Diagram for forbidden 1st order $K^+ \to \pi^+ \nu \overline{\nu}$

$\pi^+\nu\overline{\nu}$ decay. From the above discussion one notices that it represents a flavour-changing neutral current and is, therefore, forbidden.

Figure 2.3 depicts the three second order processes that contribute to the decay. Consideration of the first two of these is sufficient, as the contribution of the third diagram has been shown to be insignificant [2]. It is important to notice the internal quark lines. The diagrams beside the Feynman diagrams for the first two processes highlight the internal quark vertices present. The only constraints on the virtual quark are that they be of the up-like type (with charge 2/3). Thus the possibilities, u,c,and t, must be summed over. Now, the amplitude associated with each diagram depends on the quark mass through the propagator term as m_q^2/M^2, where M is the mass of the exchanged vector boson. If the quark masses were equal, then the only difference in the amplitudes would be due to the CKM couplings. Thus, the remainder of the amplitude could be factored out of the sum so that we would have, say, for the first diagram:

$$\mathcal{M}_1 = (\cdots) \sum_{q=u,c,t} V_{qd}^* V_{qs}$$

The summation corresponds to the inner-product of two columns of the unitary (and therefore orthogonal) CKM matrix. Hence it is identically zero. Thus, if the quark masses were equal the $K^+ \to \pi^+\nu\overline{\nu}$ branching ratio would be zero and the G.I.M mechanism would be said to be complete to all orders. Of course, the quark masses are different, and this spoils the cancellation at second order. The BR, then, obviously depends on the quark masses and the CKM matrix elements. A precise calculation was made by Inami and Lim [4] :

$$\frac{BR(K^+ \to \pi^+\nu\overline{\nu})}{BR(K^+ \to \pi^0 e^+\nu)} = \frac{\alpha^2}{8\pi^2 V_{us}^2 \sin^4\theta_W} |\sum_{q=c,t} V_{qs}^* V_{qd} D(x_q)|^2 \tag{2.2}$$

where

$$D(x) = \frac{1}{8}[1 + \frac{3}{(1-x)^2} - \frac{(4-x)^2}{(1-x)^2} x \ln(x) + \frac{x}{4} - \frac{3}{4}\frac{x}{x-1}]$$

and $x_q = m_q^2/M_W^2$.

By calculating the rate relative to the measured and similar process, $K^+ \to \pi^0 e^+\nu$, one avoids uncertainties in the hadronic wavefunctions. The calculation can be made in terms of

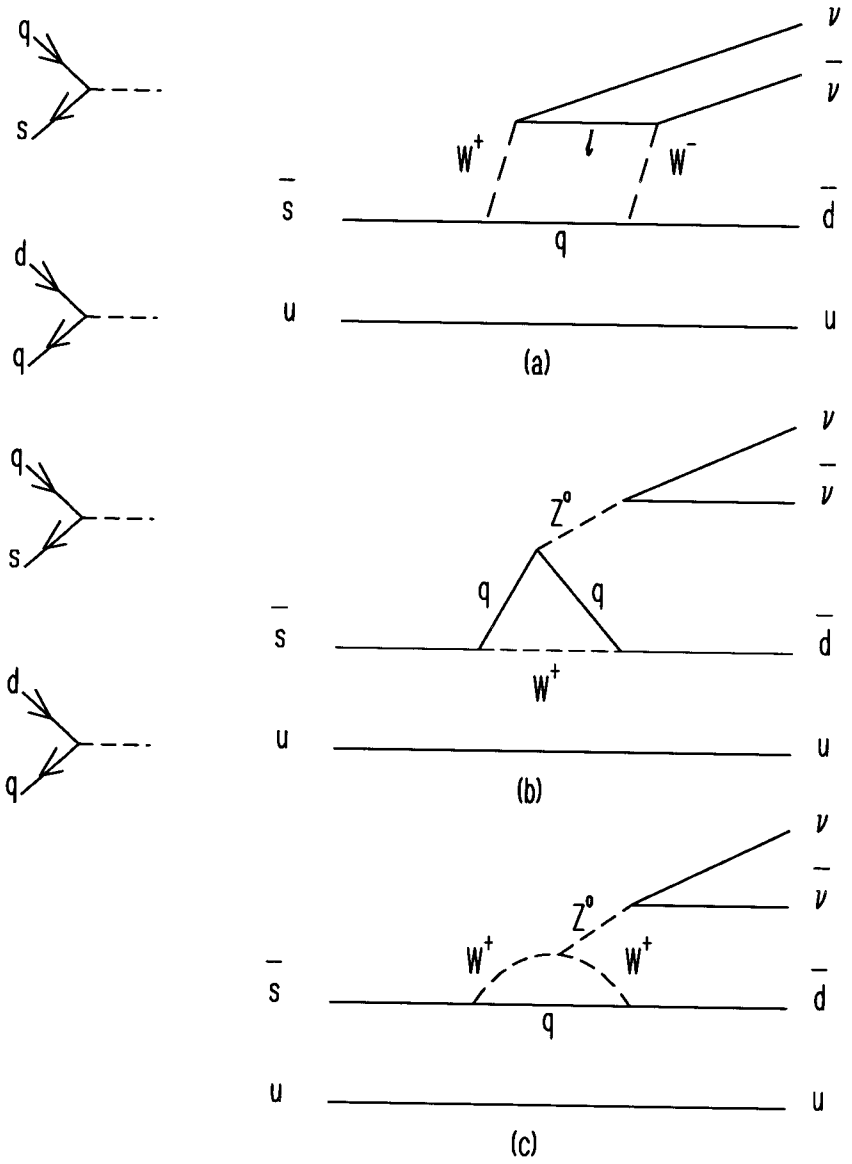

Figure 2.3: 2nd order Feynman Diagrams for $K^+ \to \pi^+ \nu\overline{\nu}$

the above process due to the similarity of the two processes in figures 2.1 and 2.2. Both have a kaon in the initial state and two leptons in the final state. The hadronic wavefunctions in the final state are related by a strong isospin rotation.

With this parameterization, the BR for three neutrino generations is found to be

$$BR(K^+ \to \pi^+ \nu\overline{\nu}) = (.6 \to 6) \times 10^{-10} \tag{2.3}$$

for the top quark mass, $m_t \simeq m_W$.

The span is due both to uncertainty in elements of the CKM matrix as well as ignorance of the top quark mass. Thus, in principle, a measurement of BR($K^+ \to \pi^+ \nu\overline{\nu}$) would allow limits to be placed on the mass of the top quark. However, if one assumes the validity of the Standard Model then a direct measurement of m_t is likely to occur before a signal is observed for BR($K^+ \to \pi^+ \nu\overline{\nu}$). In this scenario, the known value of m_t can be used to extract the magnitude of the CKM matrix element, V_{td}, as well as the value of the CP violating phase described below. The latter may be used in conjunction with values derived from other experiments to perform a detailed consistency test on the Standard Model.

Before proceeding to a discussion of the extraction of $|V_{td}|$ and the CP violating phase in sections 2.6 and 2.7, mention should be made on the possibility of observing physics beyond that predicted by the minimal Standard Model.

2.5 Window on New Physics

As will be described in the next chapter, the search for $K^+ \to \pi^+ \nu\overline{\nu}$ is, in fact, a search for $K^+ \to \pi^+ + nothing$, so that the existence of additional decay modes of a kaon into a pion and light weakly interacting particles will clearly affect the measured branching ratio.

The simplest of such extensions would be extra generations of neutrinos [32]. However, the precise effect of a fourth generation would depend on many unknown factors such as the mass of the accompanying heavy lepton.

Lepton flavour violating decays, which are strictly forbidden in the Standard Model with

massless neutrinos, comprise another possibility for new physics. These would be decays involving presently known families of leptons as decay particles, e.g, $K^+ \rightarrow \pi^+\nu_e\nu_\mu$. However, it is also possible that the additional decay modes give rise to amplitudes that interfere destructively so as to decrease the branching ratio.

Also, although in extensions of the Standard Model, the Higgs is thought to have a mass greater than $10GeV/c^2$, there is still room for a lighter Higgs with $m_H < 350MeV/c^2$ which would contribute to the branching ratio through the process $K^+ \rightarrow \pi^+ H$.

Further candidates for unobserved decay particles are light supersymmetric particles. Their existence would also have an effect on the branching ratio by introducing more amplitudes where the supersymmetric particles would replace the intermediate states in the loops in the Feynman diagrams of figure 2.3 [28, 29, 30].

Finally it should be noted that the current upper limit for $K^+ \rightarrow \pi^+\nu\overline{\nu}$ is 5.2×10^{-9} which is still at least an order of magnitude greater than the Standard Model prediction. An upper limit has also been set for the process $K^+ \rightarrow \pi^+ X^0$ where X^0 is any weakly interacting neutral particle or system thereof with mass between 150 and 250 MeV/c^2. It is dependent on the mass of the hypothetical particle but for the range mentioned is no greater than 2×10^{-7}.

2.6 Determination of $|V_{td}|$

The discussion below follows [5]. The CKM matrix of equation 2.1 may be parametrized as:

$$M_c = \begin{pmatrix} c_1 & s_1c_3 & s_1s_3 \\ -s_1c_2 & c_1c_2c_3 - s_2s_3 \exp i\delta & c_1c_2s_3 + s_2c_3 \exp i\delta \\ s_1s_2 & -c_1s_2c_3 - c_2s_3 \exp i\delta & -c_1s_2s_3 + c_2c_3 \exp i\delta \end{pmatrix} \tag{2.4}$$

where $c_i = \cos\theta_i$ and $s_i = \sin\theta_i$. That is to say, the CKM matrix may be expressed in terms of three rotation angles and a phase. Comparing this with equation 2.1 one obtains the following relations:

$$V_{td} = s_1s_2 \tag{2.5}$$

$$V_{ub} = s_1s_3 \tag{2.6}$$

and with the assumption that the cosines of small angles can be set to unity :

$$V_{cb} \approx s_3 + s_2 \exp i\delta. \tag{2.7}$$

Taking the square of the magnitude one obtains:

$$|V_{cb}|^2 = s_2^2 + s_3^2 + 2s_2 s_3 \cos\delta \tag{2.8}$$

so that

$$2s_2 s_3 \cos\delta = |V_{cb}|^2 - s_2^2 - s_3^2. \tag{2.9}$$

Using equation 2.2 for three neutrino generations and using the current values of θ_W, V_{us}, α, BR($K^+ \to \pi^0 e^+ \nu$), and expanding, one obtains the expression:

$$\begin{aligned}
\frac{K^+ \to \pi^+ \nu\overline{\nu}}{2.11 \times 10^{-6}} &= |D(x_c) + s_2(s_2 + s_3 \exp i\delta) D(x_t)|^2 \\
&= D_c^2 + 2D_c D_t(s_2^2 + s_2 s_3 \cos\delta) + D_t^2 s_2^2 |s_2 + s_3 \exp i\delta|^2 \\
&= D_c^2 + D_c D_t(|V_{cb}|^2 - s_3^2 + s_2^2) + D_t^2 s_2^2 |V_{cb}|^2 \\
&= D_c^2 + D_c D_t(|V_{cb}|^2 - s_3^2) + (D_c D_t^2 |V_{cb}|^2) s_2^2
\end{aligned} \tag{2.10}$$

where $D_c = D(x_c)$ and $D_t = D(x_t)$. Solving this equation for s_2^2 and substituting in equation 2.5 one obtains the following expression for $|V_{td}|^2$.

$$\begin{aligned}
|V_{td}|^2 = &\frac{s_1^2}{D_c D_t + D_t^2 |V_{cb}|^2} \times \\
&\left(\frac{BR(K^+ \to \pi^+ \nu\overline{\nu})}{2.11 \times 10^{-6}} - D_c \left[D_c + D_t |V_{cb}|^2 \left(1 - \left| \frac{V_{ub}}{V_{cb}} \right|^2 \frac{1}{s_1^2} \right) \right] \right)
\end{aligned} \tag{2.11}$$

It is evident from the above equation that the value of $|V_{td}|$ thus obtained will depend on other Standard Model parameters. These are :

- α and θ_c which have been absorbed into the constant 2.11×10^{-6}
- V_{ud} through $s_1^2 = 1 - c_1^2 = 1 - V_{ud}^2$
- $|V_{cb}|$ and the ratio $|\frac{V_{ub}}{V_{cb}}|$

- m_c, m_t, and m_W through the kinematic functions D_c and D_t

While the parameters in the first two items in the above list are known to good accuracy, those in the latter two are not. In fact, there has been no experimental determination of m_t to date. However, within the framework of the Standard Model, its value is constrained by the results of other experiments to lie within a certain range. An investigation of the sensitivity of the BR($K^+ \rightarrow \pi^+ \nu\overline{\nu}$) to V_{td} based on the equation 2.11 using nominal values of $m_c = 1.5GeV$ and $m_t = 200GeV$ as well as Particle Data Group central values for the remaining Standard Model parameters while ignoring uncertainties leads to the following finding. A measurement of BR($K^+ \rightarrow \pi^+ \nu\overline{\nu}$) accurate to within 20% would yield a value for $|V_{td}|$ accurate to 13%. Furthermore, the sensitivity is not a strong function of m_t. For example, at $m_t = 200GeV$, a measurement of BR($K^+ \rightarrow \pi^+ \nu\overline{\nu}$) to 25% yields $|V_{td}|$ to 17%.

A consideration of the uncertainties in Standard Model parameters in the extraction of $|V_{td}|$ modifies its uncertainty in the following manner. The uncertainties in α, θ_c, m_W, do not contribute significantly to the uncertainty in $|V_{td}|$. Although QCD corrections to BR($K^+ \rightarrow \pi^+ \nu\overline{\nu}$) cause a variation of 15% to 30% in the branching ratio, these do not translate into a large uncertainty in $|V_{td}|$. A 10% uncertainty in m_t contributes about 12% uncertainty in $|V_{td}|$. An uncertainty of $0.1GeV$ in the determination of m_c contributes about 4% to 8% uncertainty in $|V_{td}|$ depending on the value of m_t. However, unlike the uncertainty on m_t which is an experimental problem, the uncertainty in m_c is due to the theory underlying its extraction, and so is unlikely to diminish in the near future. Furthermore, although the uncertainty of 44% in the ratio $|\frac{V_{ub}}{V_{cb}}|$ contributes only 3% uncertainty to $|V_{td}|$, the 20% uncertainty in $|V_{cb}|$ contributes roughly 20% uncertainty in $|V_{td}|$. This seems to be the main source of error in the extraction of $|V_{td}|$ from BR($K^+ \rightarrow \pi^+ \nu\overline{\nu}$). It is theoretical in nature and not likely to improve in the short term. It thus sets a target of about $20 - 30\%$ for the desired accuracy of the measurement of BR($K^+ \rightarrow \pi^+ \nu\overline{\nu}$).

2.7 Determination of the CP violating phase

The discussion below follows [6]. The CKM matrix has been parametrized by Wolfenstein [7] in powers of the Cabibbo angle (to third order) as follows:

$$\begin{pmatrix} V_{ud} & V_{us} & V_{ub} \\ V_{cd} & V_{cs} & V_{cb} \\ V_{td} & V_{ts} & V_{tb} \end{pmatrix} = \begin{pmatrix} 1-\lambda/2 & \lambda & A\lambda^3(\rho - i\eta) \\ -\lambda & 1-\lambda^2 & A\lambda^2 \\ A\lambda^3(1-\rho-i\eta) & -A\lambda^2 & 1 \end{pmatrix} \tag{2.12}$$

where $\lambda = \sin\theta_c \simeq 0.22$.

Substituting this parameterization of the CKM matrix into the theoretical expression for $\mathrm{BR}(K^+ \to \pi^+\nu\overline{\nu})$ of equation 2.2 one obtains the following relation.

$$\frac{BR(K^+ \to \pi^+\nu\overline{\nu})}{BR(K^+ \to \pi^0 e^+\nu)} \frac{8\pi_2 \sin\theta_W{}^4}{3\alpha^2} \frac{1}{A^4\lambda^8 D_t^2} = \eta^2 + \left(1 + \frac{(1-\lambda^2/2)}{A^2\lambda^4}\frac{D_c}{D_t} - \rho\right)^2 \tag{2.13}$$

This describes a circle in the complex $\rho - \eta$ plane centred at :

$$1 + \frac{(1-\lambda^2/2)}{|V_{ts}|^2}\frac{D_c}{D_t} \tag{2.14}$$

and with a radius of :

$$\frac{1}{|V_{ts}|^2 D_t}\sqrt{\frac{BR(K^+ \to \pi^+\nu\overline{\nu})}{2.11 \times 10^{-6}}} \tag{2.15}$$

where the following numerical values have been used: $BR(K^+ \to \pi^0 e^+\nu) = 0.0483$, $\sin\theta_W = 0.23$, and $\alpha = 1/128$.

Therefore, a measurement of $\mathrm{BR}(K^+ \to \pi^+\nu\overline{\nu})$ determines a circle in the $\rho - \eta$ plane with centre on the real, ρ, axis and displaced slightly from the point (1,0) by the charmed quark contribution to the branching ratio. It should be noted that the kinematic functions, D_c and D_t, are both monotonically increasing functions of their respective quark masses. The displacement of the circle centre from the origin as well as its radius both decrease with increasing $|V_{ts}|$ or D_t, and hence increasing m_t. The radius grows as the square root of the measured branching ratio. QCD radiative corrections to $\mathrm{BR}(K^+ \to \pi^+\nu\overline{\nu})$ have been calculated. There effect is to scale the charmed quark contribution, D_c, by 0.71. This does not change the type of curve obtained

in the $\rho - \eta$ plane, nor does it have an effect on the radius of the circle. It does, however, reduce the displacement of the centre from (1,0) by that same factor.

Their remains the fact that the top quark mass is still unknown and that $|V_{ts}|$ is the CKM parameter with the greatest degree of uncertainty (20%) after V_{td}. However, taking the limit of the PARTICLE DATA GROUP fit for $|V_{ts}|$ as well as the lower limit on m_t from the CDF collaboration [8] of $89 GeV/c^2$, one can calculate an upper limit on the radius as well as an upper limit on the displacement of the centre from the point (1,0) along the real axis. Thus, an oval region in the $\rho - \eta$ plane is circumscribed within which must fall the value chosen by nature. As the measurement of the upper limit on the BR($K^+ \rightarrow \pi^+ \nu\overline{\nu}$) improves the region of allowed values becomes smaller.

2.7.1 Consistency of Standard Model parameters

Other constraints on the allowed region in the $\rho - \eta$ plane also exist. A review of such constraints by Kim, Rosner, and Yuan [10] included the following:

- The magnitude, $|\frac{V_{uc}}{V_{cb}}|$, which, with 1σ errors, defines an annular region centred on the origin.
- Circles centred on the point (1,0) with radius varying with top quark mass, determined by $B - \overline{B}$ mixing.
- Hyperbolas with a common focus at (1,0) determined by the parameter , ϵ which describes the main features of CP violation in the Kaon system.

Figure 2.4 shows the curves based on central values of the above quantities as well as those derived from the experimental 1σ uncertainties. That is to say that uncertainties in other Standard Model parameters have not been included in the uncertainties displayed in the figure.

When the upper limit on BR($K^+ \rightarrow \pi^+ \nu\overline{\nu}$) approaches the Standard Model predicted range it will appear on the figure as an oval region. Furthermore, when the mass of the top quark is known and when an actual measurement of BR($K^+ \rightarrow \pi^+ \nu\overline{\nu}$) is obtained, it can be displayed

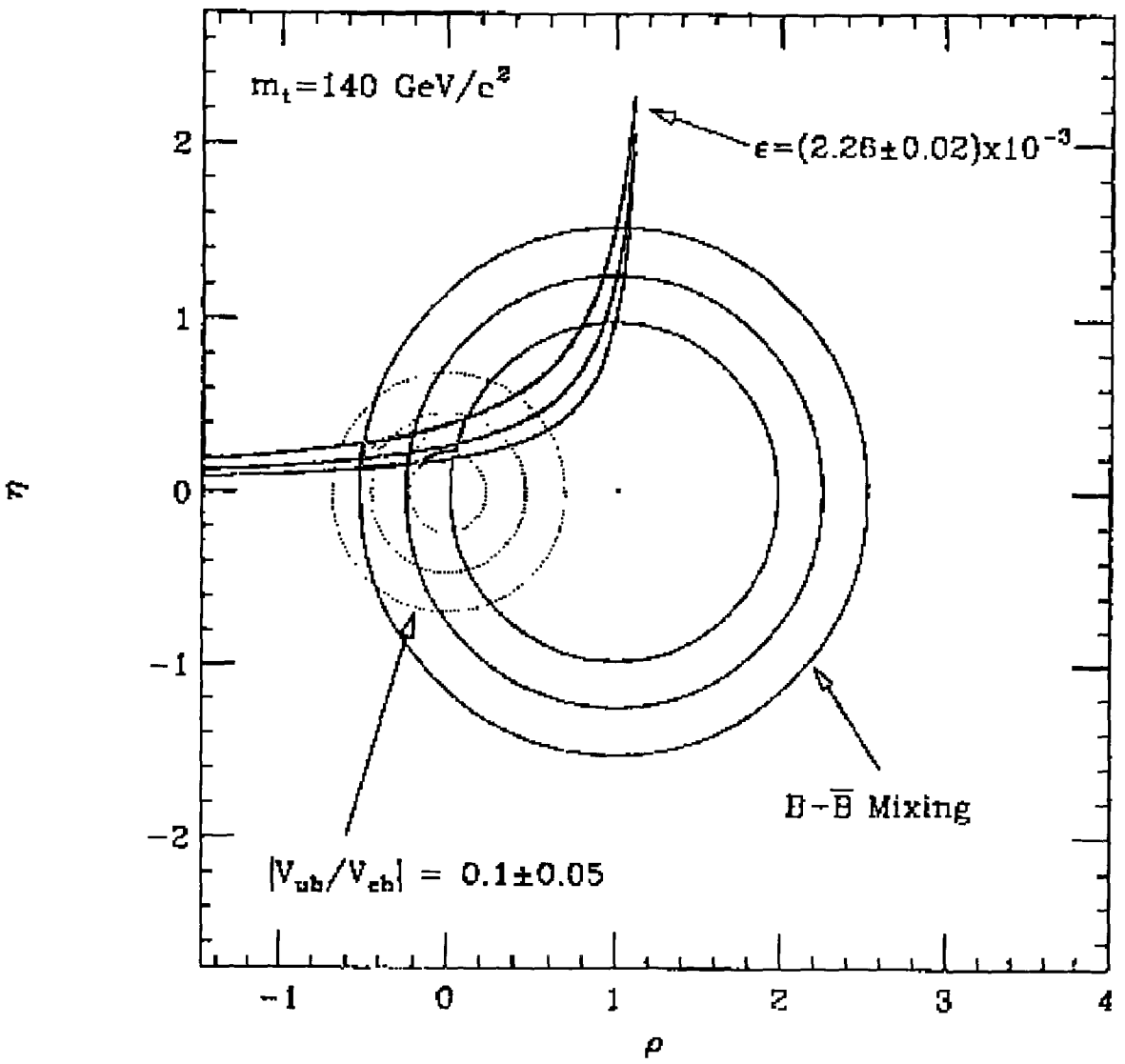

Figure 2.4: Constraints in ρ — η Plane from Experiment

on the graph in figure 2.4 as an annular region along with the previous results to see if the three generation Standard Model is adequate to explain the results of all of these experiments.

The region defined by the measurement of BR($K^+ \rightarrow \pi^+ \nu\overline{\nu}$) will be subject to the following uncertainties:

- Statistical and systematic error in the experiment. An estimate for the uncertainty in the acceptance of the detector is 10% [9]. Thus, there is not much motivation for achieving a statistical error much better than that. One could therefore envisage a measurement of BR($K^+ \rightarrow \pi^+ \nu\overline{\nu}$) accurate to 20%.

- Uncertainty in the top quark mass. A 1% uncertainty has been estimated for m_t assuming the top quark is discovered at SSC with a mass between 89 and $200GeV$.

- Uncertainty in the value of $|V_{ts}|$. The latter is equivalent to $|V_{cb}|$ and the its error is dominated by theoretical uncertainties. It is estimated to be 10 - 20% [10], which translates directly into an error on the displacement and radius.

Figure 2.5 shows the central value and 1σ limits due to the variation in $|V_{ts}|$ for a top quark mass of $140GeV/c^2$ and an imagined measured BR($K^+ \rightarrow \pi^+ \nu\overline{\nu}$) of 2×10^{-10}. Comparing the scales of figures 2.4 and 2.5 it would seem that a 20% measurement of BR($K^+ \rightarrow \pi^+ \nu\overline{\nu}$) is both adequate and interesting.

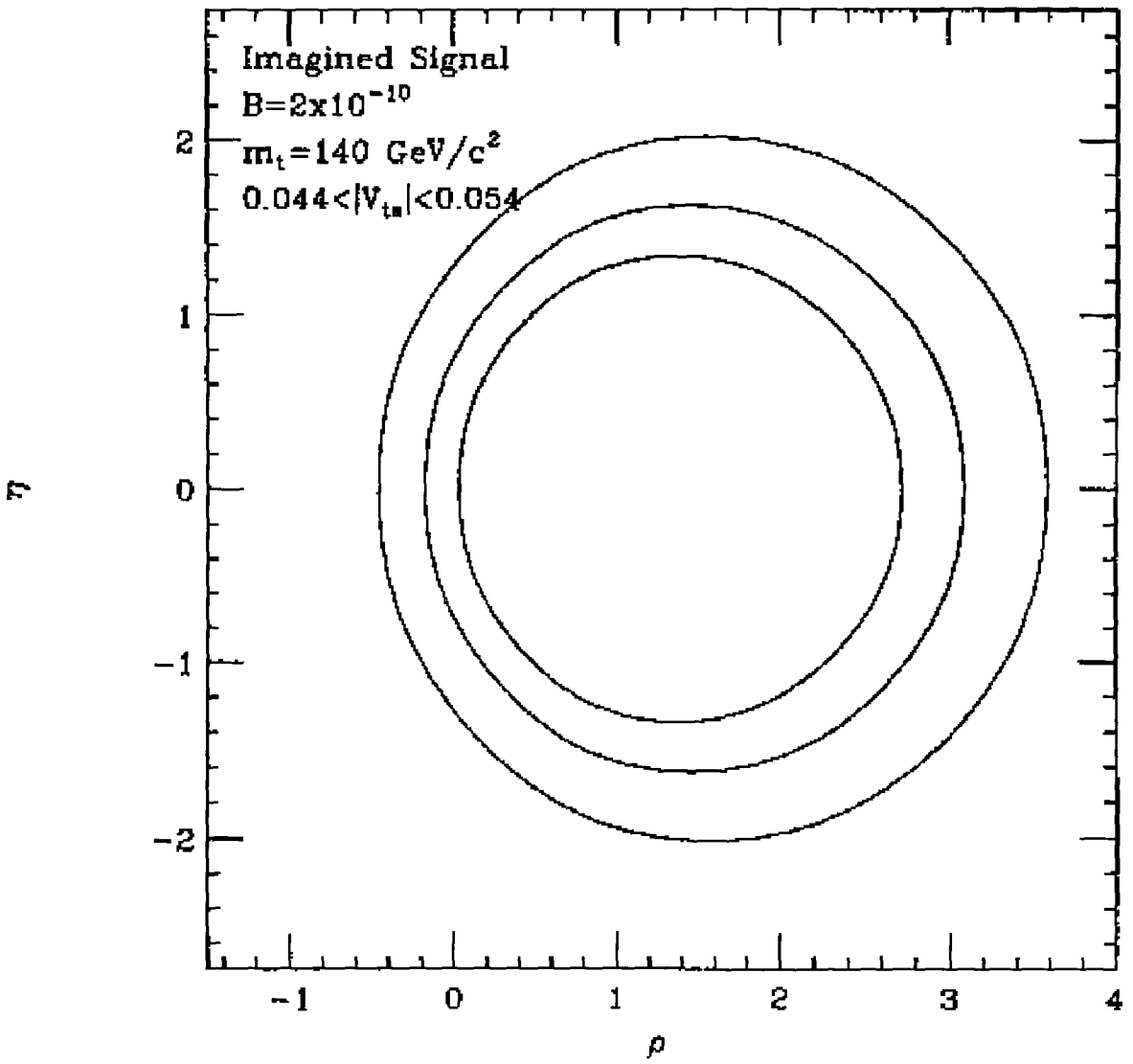

Figure 2.5: Constraints in ρ — η Plane with $K^+ \to \pi^+ \nu\overline{\nu}$ Measurement

Chapter 3

Experiment Overview

3.1 Introduction

Since neutrinos are exclusively weakly interacting they are, for all practical purposes, directly unobservable. Consequently, the search for the decay $K^+ \to \pi^+\nu\overline{\nu}$ is, in effect, a search for the decay $K^+ \to \pi +$ nothing. Any real detector system is prone to misidentifying or missing emerging particles. Moreover, since $K^+ \to \pi^+\nu\overline{\nu}$ is a rare process, it will be accompanied by backgrounds leaving similar signatures in the detector at very high rates. The combination of the above two facts poses serious difficulties in making an unambiguous measurement of the decay $K^+ \to \pi^+\nu\overline{\nu}$.

This chapter first briefly describes the method used by the E787 collaboration to search for the rare decay $K^+ \to \pi^+\nu\overline{\nu}$. It then proceeds to examine in greater detail the background processes and describes the manner in which they can confound the measurement.

3.2 Strategy

The general strategies used to overcome the difficulties mentioned above are kinematics, effective particle identification, and extremely efficient photon detection. The tools used in implementing these strategies are those that are standard in nuclear and particle physics, a beam of accelerated particles, a target, drift chambers, scintillation detectors, high speed electronics and computing power. Furthermore, the implementation of these strategies is greatly facilitated by the simplifying assumption that the decaying kaon is at rest. This assumption is rendered valid by using an active target to stop a beam of kaons and requiring a time delay between the kaon and the appearance of the pion. This requirement for triggering is called "delayed coincidence". The stopped kaon ensures the monochromatic nature of the spectrum of the charged particle from the two–body decays, $K_{\pi 2}$ and $K_{\mu 2}$ described below. It also fixes the initial momentum and energy which allows one to make the assumptions described in the subsections below.

3.2.1 Kinematics

The following processes comprise the background in the measurement of $K^+ \rightarrow \pi^+\nu\bar{\nu}$:

1. $K_{\pi 2}$: $K^+ \rightarrow \pi^+\pi^0 \rightarrow\ 2\gamma$ (BR 0.21)
2. $K_{\mu 2}$: $K^+ \rightarrow \mu^+\nu_\mu$ (BR = 0.64)
3. scattered beam π^+
4. $K^+ \rightarrow \mu^+\nu_\mu\gamma$ (BR = 0.0055)
5. $K^+ \rightarrow \pi^0\mu^+\nu_\mu$ (BR =0.032)
6. $K^+ \rightarrow \pi^0 e^+\nu_e$ (BR = 0.048)
7. $K^+ \rightarrow \pi^+\pi^+\pi^-$ (BR = 0.017)
8. $K^+ \rightarrow \pi^+e^+e^-$
9. $K_{\pi 3}$: $K^+ \rightarrow \pi^+\pi^0\pi^0$
10. $K^+ + n \rightarrow\ p + K_L^0;\ \ K_L^0 \rightarrow \pi^+e^-\nu$

Figure 3.1 shows the momentum spectrum of the principal background modes as well as the sought rare processes. The numbers in parentheses give their respective branching ratios. The method used and the design of the detector itself are both motivated by the rejection of these backgrounds. The modes $K_{\mu 2}$ and $K_{\pi 2}$, with branching ratios of 0.64 and 0.21 respectively are of particular concern. By confining the search to the region between the $K_{\mu 2}$ and $K_{\pi 2}$ peak, or $213 < \frac{P_\pi}{(MeV/c^2)} < 237$, a high degree of background rejection is achieved while still accepting about 20% of the phase space. Figure 3.2 and Figure 3.3 depict the spectrum of the range in scintillator and of total energy for the same processes. The kinematic separation between the $K_{\pi 2}$ and $K_{\mu 2}$ peak is even greater than for the momentum. Similar cuts are made on the basis of energy and range, and events are depicted on a three dimensional cartesian plot of energy, range, and momentum. The kinematic limits due to the $K_{\pi 2}$ and $K_{\mu 2}$ peaks on each axis define

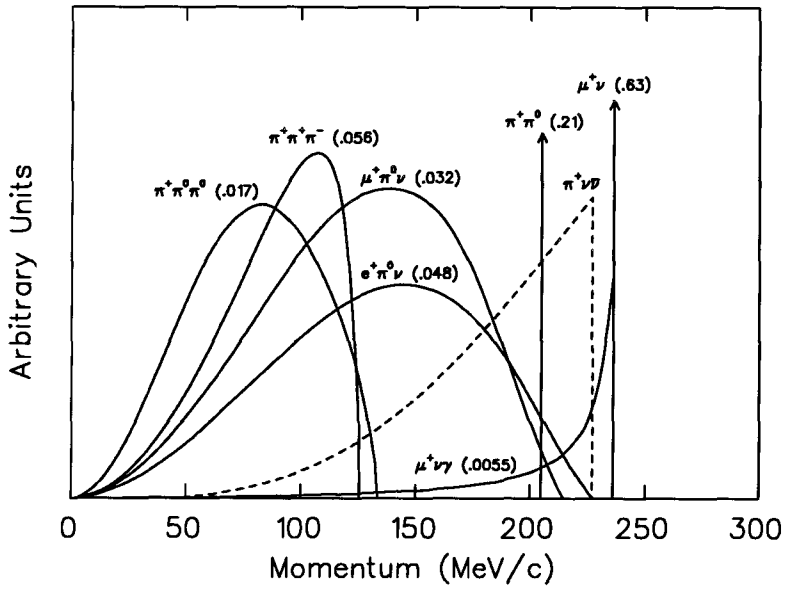

Figure 3.1: Momentum spectrum of rare and background K^+ decays

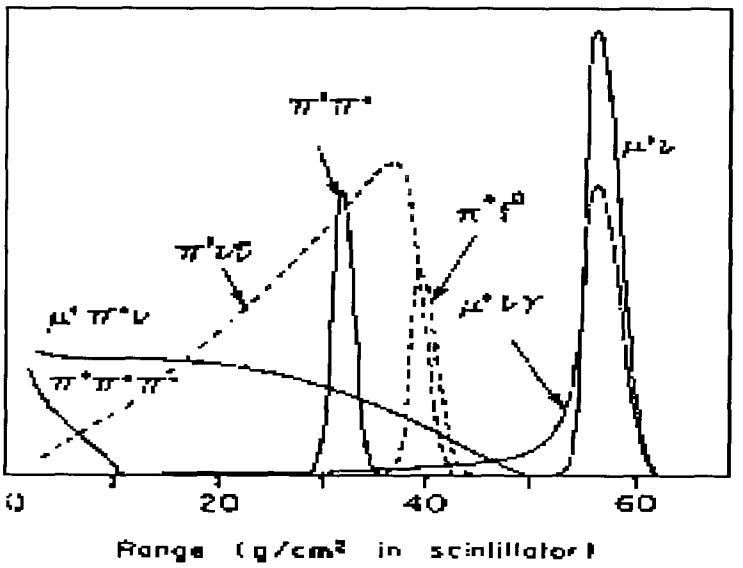

Figure 3.2: Range spectrum of rare and principal allowed K^+ decays

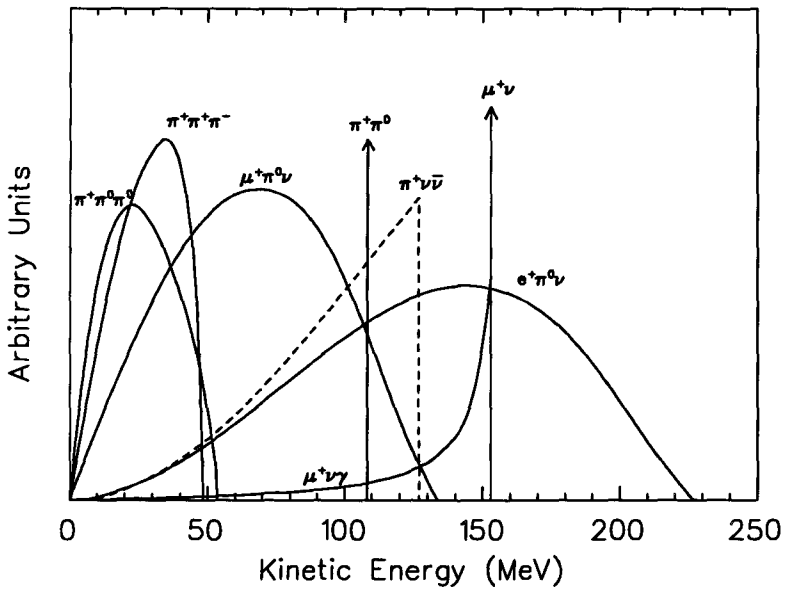

Figure 3.3: Energy spectrum of rare and principal allowed K^+ decays

a box in this three-dimensional space. Events are then said to fall inside or outside the box with an event inside the box representing a signal for the decay.

3.2.2 Particle Identification

Particle identification is achieved in two completely different ways. The first involves combining the measurements of particle momentum and range to test a particle mass hypothesis, while the second consists of observing the decay chain $\pi^+ \rightarrow \mu^+ \rightarrow e^+$.

Range–Momentum

The average differential energy loss per unit length due to Coulomb interactions of a particle travelling through a medium is given by the equation shown below called the *Bethe–Block* equation:

$$\frac{dE}{dX} = -K\frac{Z}{A}\frac{\rho}{\beta^2}\left\{\ln\frac{2mc^2\beta^2 E_M}{I^2(1-\beta^2)} - 2\beta^2\right\} \tag{3.1}$$

with

$$K = \frac{2\pi N z^2 e^4}{mc^2}$$

where N is Avogadro's number, m and e are the electron mass and charge, Z,A, and ρ are the atomic number, atomic mass, and density of the medium, respectively, and I is its effective ionization potential; z is the charge and β the velocity (in units of the speed of light) of the ionizing particle. The quantity E_M is the maximum energy transfer allowed in each interaction. Simple relativistic two–body kinematics yields that $E_M = 2mc^2\beta^2/(1-\beta^2)$.

For a given particle type and medium, the rate of energy loss can be rewritten as a function of particle velocity only:

$$\frac{dE}{dX} = \lambda_v(v). \tag{3.2}$$

The kinetic energy of a particle of mass M is $E_K = M\epsilon(v)$, where $\epsilon(v)$ is a function of velocity only. Therefore, by inverting $\epsilon(v)$ and substituting for v in equation 3.2 one can write the energy loss in terms of E and M :

$$\frac{dE}{dX} = \lambda_E(E/M). \tag{3.3}$$

Hence the range of the particle may be obtained by integrating the above equation from the starting kinetic energy to zero. The predicted range will depend upon the type of particle one assumes through the variable M. To denote this the variable M is replaced by M_i with $i = \mu, \pi$ depending on the hypothesis. The predicted range for a given hypothesis is given by:

$$R_i^{pred} = \int_{\sqrt{p_{DC}^2+M_i^2}-M_i}^{0} \frac{dE}{\lambda_E(E, M_i)} \tag{3.4}$$

where p_{DC} refers to the momentum as measured before entry into scintillator.

A Gaussian distribution of the measured ranges about the predicted range (plus an offset, δ_R due to systematic measurement errors) is assumed. A likelihood function of the form

$$L_i = \exp \frac{(R_i^{pred} - R_i^{meas} - \delta_R)^2}{2\sigma_R} \tag{3.5}$$

is calculated for each hypothesis (pion,muon). The particle is identified as the one corresponding to the hypothesis with the greater likelihood. Moreover, cuts are made requiring threshold values of the relative likelihood, L_π/L_μ, for accepting candidate stopped particles as pions.

TD Waveform Fitting

This is a method of distinguishing between muons and pions. A more detailed description of the detector components is given in chapter 4, however, for the purposes of this section it is suffient to know that the target, (and central tracking drift–chamber) are surrounded by a series of scintillating elements collectively known as the range stack. Light is collected from the scintillator by photomultiplier tubes which are instrumented with transient digitizers (TD's) which record the output waveforms.

Particle identification is achieved based on the following effect. A stopped π^+ will decay via the process $\pi^+ \rightarrow \mu^+\nu_\mu$. A μ^+ will decay via $\mu^+ \rightarrow e^+\nu_e\overline{\nu_\mu}(\gamma)$. Since particles deposit a large portion of their energy just before stopping, a large pulse is observed in the photomultiplier output when the pion stops in the scintillator. It then decays to a $4.12MeV$ μ^+. The muon will, in turn, stop in the same scintillating element producing a second, smaller pulse. The stopped muon then decays into a positron. However, the positron—muon mass difference is large so that the emerging positron will have sufficient energy to escape the element in which it originated and register hits in adjacent elements.

Therefore, in order for a hit in the range stack to be identified as pion the following criteria are sought. The pulse shape from the original stopping element must have two peaks — one for the pion stopping and one for the muon stopping. In addition, energy must be deposited in adjacent elements to show evidence of the $\mu^+ \rightarrow e^+$. The latter requirement provides further rejection of backgrounds where the first, double pulse was due to a $\mu^+ \rightarrow e^+$ decay followed by an accidental hit.

3.2.3 Photon Veto

The $K_{\pi 2}$ decay is a two-body decay with the π^+ and π^0 emerging back to back with well-defined and roughly equal energies and momenta. As the π^0 does not interact via the Coulomb interaction and, as its lifetime is too short to allow its detection directly, the principal method for detecting it and thus suppressing the background due to the $K_{\pi 2}$ is the detection of the photons that emerge from its subsequent decay. The two photons from the decay range in energy from 20 to 225 MeV. However conservation of energy yields that if one photon is of low energy and difficult to detect the other will be of high energy and easily detectable. Furthermore, conservation of the π^0 momentum guarantees that there be at least one energetic photon with its momentum roughly parallel to that of the parent π^0 and therefore anti-parallel to the π^+ from the kaon decay.

The same principle holds true for $K_{\pi 3}$ decays as well, although in a more complicated manner and to a lesser extent. The daughter particles from this decay are a π^+ and two π^0's. If the π^+ is not energetic then the event will fail the kinematic requirement, therefore, in the following it is assumed that the π^+ has significant energy and momentum. By conservation of momentum, there must therefore be at least one energetic π^0 with momentum anti-parallel to that of the π^+. From there the reasoning proceeds as for the $K_{\pi 2}$ case to guarantee that there be at least one energetic photon anti-parallel to the π^+.

Although the entire detector is encased in scintillator dedicated to photon vetoing over 4π of solid angle, the anti-correlation of the photon momentum with that of the π^+ allows one to make use of other scintillating elements by vetoing also on the basis of all energy collected in time with the kaon decay but spatially separated from the charged track.

3.3 Backgrounds

3.3.1 $K_{\pi 2}$: $K^+ \to \pi^+\pi^0$

Since the charged particle is in fact a π^+ just like for $K^+ \to \pi^+\nu\overline{\nu}$, the only qualitative difference is the detection of the photons from the subsequent π^0 decay. Therefore, background arises due to the photon detection inefficiency. However, to further suppress backgrounds kinematic cuts are made on momentum, range, and energy which suppress $K_{\pi 2}$ by a factor of 10^5 but reduce the acceptance by a factor of 1.5×10^{-3}. This represents an improvement in signal to noise by a factor of 150.

3.3.2 $K_{\mu 2}$: $K^+ \to \mu^+\nu_\mu$

Given the discussion of muon and pion particle identification given in the previous section, in order for a $K_{\mu 2}$ background event to appear the following must occur. The muon range in scintillator must be measured in the range $35 - 42\ g/cm^2$ (see figure 3.2). There must be no photons detected. After the initial stopping pulse, either an accidental pulse must simulate the two–peak shape of $\pi^+ \to \mu^+ \to e^+$ decay chain or the muon must decay to a $4MeV$ electron and another, accidental decay must occur to simulate the $\pi^+ \to \mu^+ \to e^+$ sequence.

3.3.3 Scattered beam pions

This background arises from the difficulty of producing pure K^+ beams. The ratio of pions to kaons in the purest of beams is about two to one. Hence, backgrounds arise when a beam π^+ arrives in the target just after the kaon and scatters into the tracking volume giving the appearance of a decay product.

3.3.4 $K^+ \to \mu^+\nu_\mu\gamma$

This process is similar to its non-radiative cousin, $K^+ \to \mu^+\nu_\mu$, and so will arise under the same conditions plus that of failure to detect the emerging photon. It is interesting to note, however,

that suppression of this background is aided by the following effect. At high muon momentum, the process is almost exactly like $K_{\mu 2}$ decay where events are suppressed through particle identification and kinematics, with the low–energy photon being difficult to detect and of little consequence. As the muon momentum decreases, the kinematical suppression decreases but the corresponding increase in the photon momentum due to momentum conservation facilitates the photon vetoing.

3.3.5 $K^+ \to \pi^0 \mu^+ \nu_\mu$

This background can arise from misidentification of the muon as a pion combined with the failure to detect the photons from the subsequent π^0 decay. It thus bears resemblance to $K_{\pi 2}$ and $K_{\mu 2}$ backgrounds except that it is a three-body decay and hence not monochromatic. This hinders suppression of it through purely kinematical considerations. However, the advantage of redundancy is gained in that both photon vetoing and muon identification are applicable.

3.3.6 $K^+ \to \pi^0 e^+ \nu_e$

This background is very similar to $K^+ \to \pi^0 \mu^+ \nu_\mu$ except that misidentification of the electron's charged track as that of a pion is less likely.

3.3.7 $K^+ \to \pi^+ \pi^+ \pi^-$ and $K^+ \to \pi^+ e^+ e^-$

This background is easily identifiable by the multiplicity of charged tracks. Due to conservation of momentum, the stopped kaon requirement precludes the production of a sole long-distance charged track. Only two out of potentially three charged tracks need be detected. In fact detection of a single charged track may be sufficient to distinguish this from $K^+ \to \pi^+ \nu \overline{\nu}$ if that track is due to the π^- with its negative curvature in magnetic field.

3.3.8 $K^+ \to \pi^+\pi^0\pi^0$

This background is similar to $K_{\pi 2}$ except, once again, in that it is not monochromatic. This kinematical disadvantage is offset by the fact that there are potentially twice as many photons to detect.

3.3.9 $K^+ + n \to p + K_L^0$; $K_L^0 \to \pi^+ e^- \nu$ nuclear reaction in stopping material

The combination of kaon charge exchange followed by a semi-leptonic decay can give rise to backgrounds according to the following scenario. The incoming K^+ undergoes kaon charge exchange as it interacts with a neutron in the nucleus of the stopping material producing a low–energy proton. The low–energy proton goes undetected as it may not even by emitted from the nucleus. The K_L^0 lives for a while then decays to simulate the delayed coincidence trigger giving rise to a low–energy electron which goes undetected (along with the neutrino). The long–range π^+ recoiling off the leptons could then be mistaken as having emerged from the process $K^+ \to \pi^+ \nu\overline{\nu}$.

Chapter 4

The Detector

4.1 Introduction

This chapter provides a brief general description of the entire detector used by the E787 collaboration to measure the branching ratio of $K^+ \to \pi^+\nu\overline{\nu}$. The first section gives an overview of the entire system, and the sections that follow it briefly describe the various sub–systems.

4.2 Overview

A low-energy separated beam line (LESB I) provides a source of charged kaons which pass though a fine-grained multi-wire proportional chamber and a series of scintillators and hodoscopes used to define the beam. These particles of approximately $800 MeV/c$ are slowed by a beryllium–oxide degrader. A Čerenkov counter before the degrader establishes particle type which is confirmed by a dE/dX measurement after the degrader. The particles stop in a highly segmented scintillating fiber target which sits in the centre of a cylindrical composite detector entirely contained in a conventional solenoidal magnet. The magnet provides a uniform $10kG$ field pointing in the positive z–direction which is parallel to the direction of flow of the beam and collinear with the axis of cylindrical symmetry of the detector. Figure 4.1 provides a cut–away view of the detector and figure 4.2 is a scale drawing of the configuration of the sub-systems circa the 1990 experimental run.

Decay products emerging within a 2π solid angle are tracked in a drift chamber before entering the range stack. This is a cylindrical shell of plastic scintillator segmented both azimuthally and radially. The pulse shape from the element in which the decay particle stops, in itself, provides a basis for particle identification as explained in section 3.2.2 In addition the rudimentary level of tracking provided by the segmentation, which is augmented by two layers of thin cylindrical multi-wire proportional chambers (RSPC's) interspersed between layers of scintillator, is sufficient for a range measurement which also serves as a basis for particle identification.

Finally, the range stack is enclosed by a barrel–shaped electromagnetic calorimeter made of

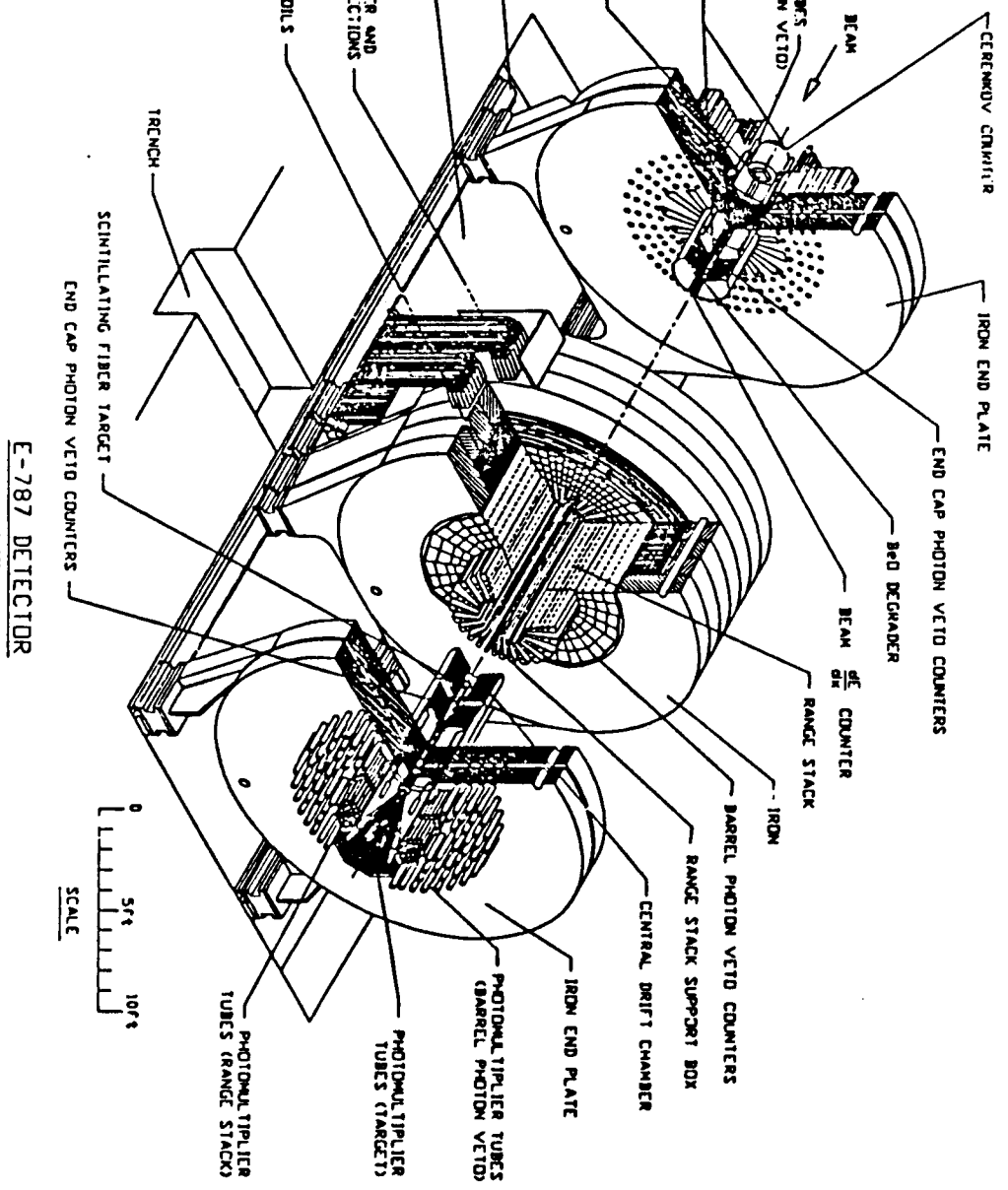

Figure 4.1: Cut–away view of E787 detector

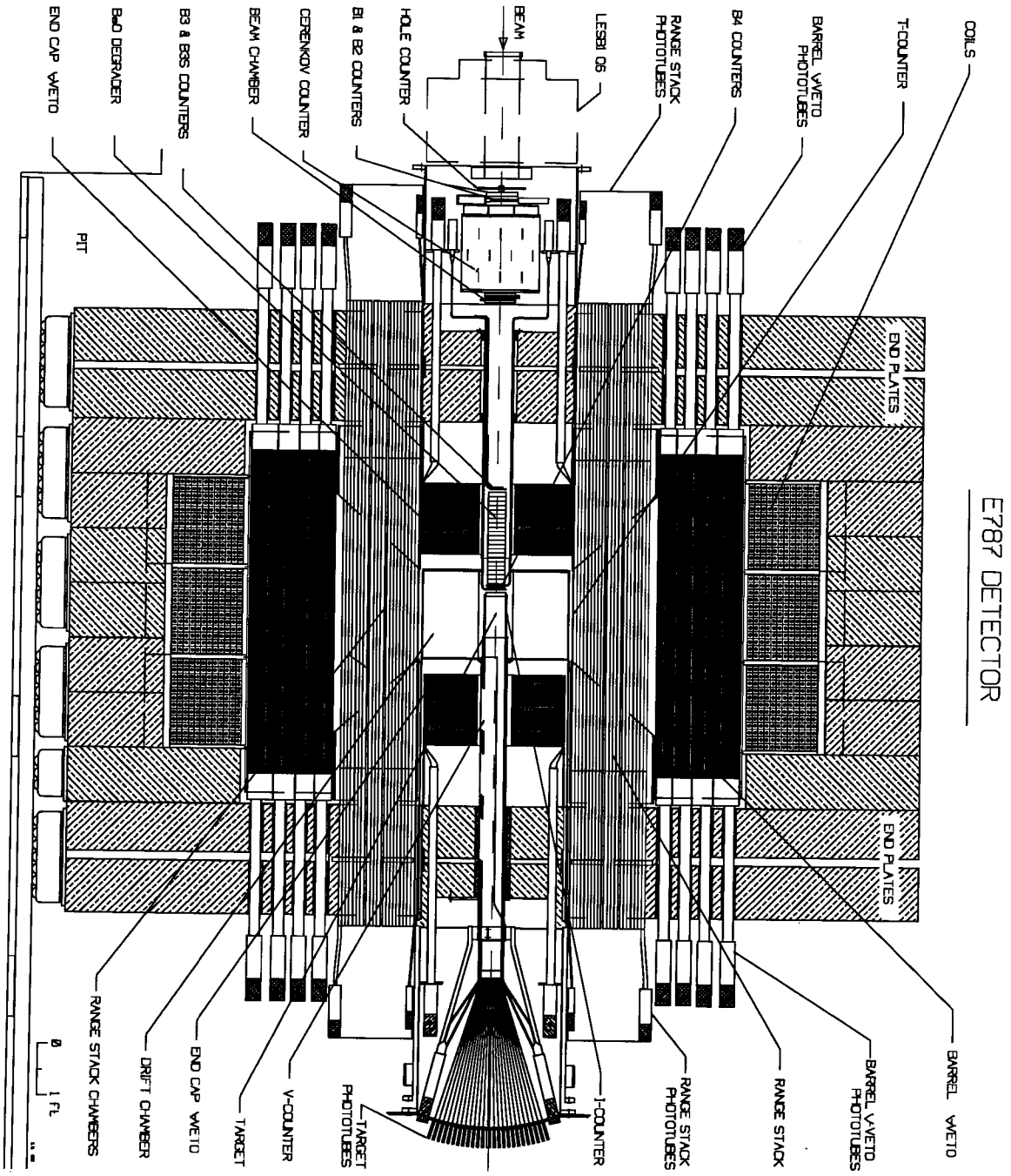

Figure 4.2: Scale drawing of E787 detector

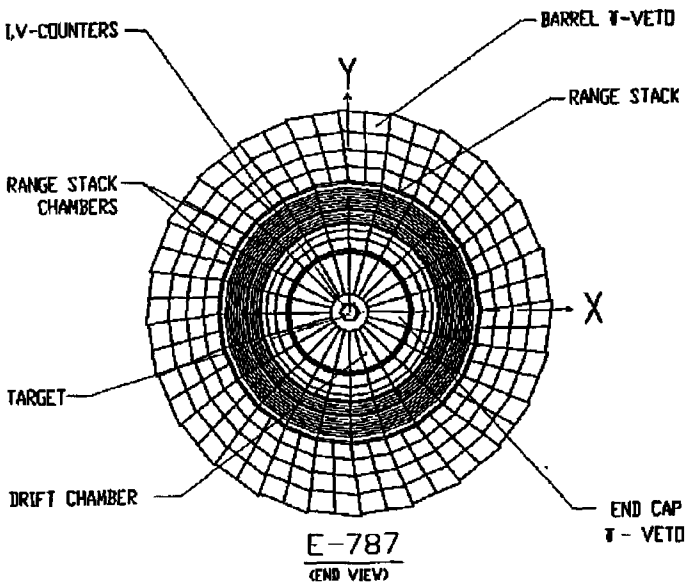

Figure 4.3: Endview of detector

lead–scintillator sandwich and two-endcaps providing almost 4π coverage of photon detection. Figure 4.3 shows and endview of the detector depicting the various elements mentioned above.

4.3 The Beam

The beam of K^+'s is produced in the following fashion. A beam of 28 GeV protons extracted slowly from the Alternating Gradient Synchrotron (AGS) is made to strike a platinum target thereby producing a plethora of secondary particles. Among these particles are protons,

lambdas, pions, and, of course, kaons. Low energy particles produced at 10.5^o with respect to the incident beam are extracted by a dipole magnet. Two quadropole magnets then focus the beam onto a second dipole that spatially disperses the particles according to momentum. The beam then passes through an electrostatic separator. This is a device using crossed electric and magnetic fields to transform the one–dimensional spatial dispersion of the particles in the beam with respect to momentum into two-dimensions with respect to particle mass and velocity. Two more quadropole magnets focus this dispersed beam onto the mass slit which selects particles by transmitting only particles in a narrow mass band. A final pair of quadropoles focuses the selected particles into the detector. The length of the beamline is 15.5 meters. By this method it has been possible to produce beams with one kaon for every two pions.

The slow extraction of the primary AGS beam leads to $2–3 \times 10^5$ kaons stops in the target distributed smoothly in time over 1.4 seconds. This low instantaneous rate is important because it does not flood the detector and electronics. Barring an accidental pile-up, this rate ensures that the detector is tracking only one kaon at a time.

4.4 The beam counters

The beam counters define the geometrical acceptance into the detector for beam particles and they provide the accurate timing information for triggering. In addition, they serve as a diagnostic for tuning the beam. The system of beam counters is depicted in figure 4.4 below. It consists of four scintillating detectors, B1 – B4, a multi-wire proportional chamber (MWPC), and a Čerenkov counter.

B1 is a simple scintillation counter placed immediately downstream of the final quadropole beam–focusing magnet and is used for beam tuning. It is followed downstream by B2, also used for beam tuning, which is a hodoscope. B3 is composed of two concentric scintillator discs of different radii placed one after the other. A comparison of their rates provides a measure of the tightness of focus of the beam before entry into th degrader. B4 is a three-layer scintillation detector. Two of the layers make up a X – Y hodoscope and the final layer, just before the

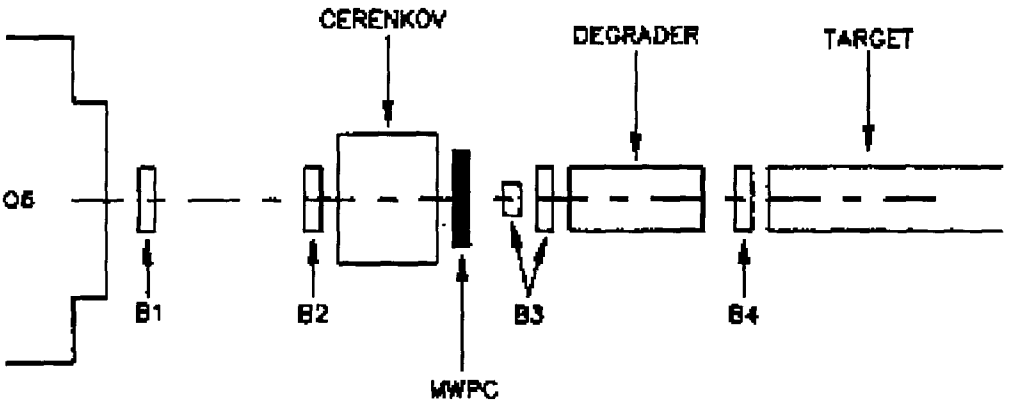

Figure 4.4: Schematic representation of beam counters

target, provides part of the beam signal for triggering. Also, photons produced from a decay in the target escaping in the upstream direction will register a hit in B4 in coincidence with the charged track. Thus, this counter also serves to plug what would otherwise be a hole in the photon veto in the upstream direction. The hodoscope part of the counter, in addition to providing information on the beam particle multiplicities, provides a dE/dX measurement based on the pulse height by exploiting the different ionization rates for pions and kaons. This provides confirmation of beam particle identification just before entering the target.

The initial beam particle identification is provided by the Čerenkov counter. In the momentum band 750 – 800 MeV/c kaons and pions produce Čerenkov light in lucite which lie on either side of the critical angle for internal reflection. Pion light produced at the shallower angle is internally reflected, leaves by the side of the disc where it is collected by a conical mirror and reflected onto the PMT's recording pions. The light from the kaon is emitted forward, leaves the downstream end of the disc and is reflected by a parabolic mirror onto PMT's recording kaons. This is depicted in figure 4.5 below. Immediately downstream of the Čerenkov counter is a three–layer MWPC that serves as a check on the beam profile before entry into the degrader and provides redundancy on beam particle multiplicity.

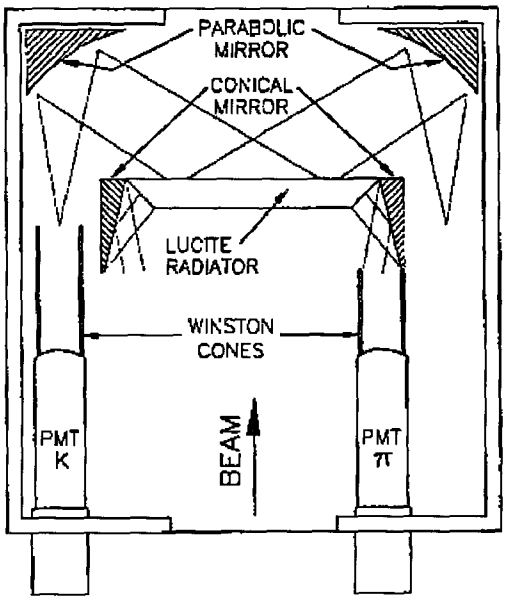

Figure 4.5: The Čerenkov counter

4.5 The Target

The kaons stop in a live fiber target consisting of 378 triangular scintillating elements arranged in a hexagonal array. Each element is composed of six fibers, 2 millimeters in diameter and 3 meters in length, which have been glued together. One ADC and one TDC per six fiber cluster, or triangle, serve to record the scintillation light pulse shapes.

The spatial segmentation of the target as well as the good timing information allow for early tracking of decay particles and hence reconstruction of the decay vertex. This helps to flag events having a detached vertex where the apparent decay pion did not emerge from the charged kaon, as happens in the case of kaon charge exchange backgrounds and scattered pion backgrounds. Also, it is the good timing information that makes possible the implementation of the "delayed coincidence" requirement of a time delay between the kaon entering the detector and the appearance of the pion.

The fiducial volume of the target is defined by two additional scintillation detectors, the

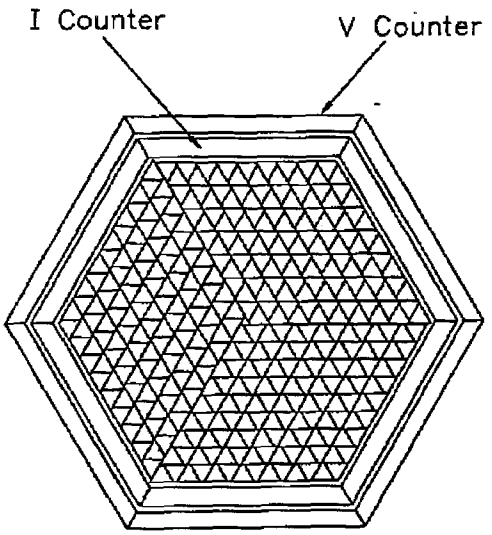

Figure 4.6: Cross–sectional view of the target

I–counter and the V–counter. These are shown in figure 4.6. By requiring a hit in the I–counter and no hit in the V–counter a limit is placed on the maximum amount of obliqueness of an acceptable track emanating from the target. This is done to validate the rough measurement of the range obtained from the range stack (described in section 4.7) based on the stopping layer of the track.

4.6 The Drift Chamber

The drift chamber occupies the region between the target and the range stack. Its primary purpose is to measure the momentum of the decay particle.

The existing drift chamber consists of 5 radial layers with each layer being azimuthally segmented into 36,40,50,60, and 70 cells respectively from inner to outer layer. The first, third, and fifth layers have six instrumented anode wires oriented axially. The second and fourth layers have six wires oriented at angles from 3.1 to 4.0 degrees with respect to the axis of the

chamber. The drift gas used was an argon,ethane, ethanol mixture in the ratio 49.9:49.9:0.2 at atmospheric pressure.

This existing chamber will be replaced by the UTC which is the main topic of this thesis and discussion of it is deferred to the next chapter where it is presented in some detail.

4.7 The Range Stack

As its name suggests the range stack provides the first quick estimate of the range of emerging decay products. In addition to this, however, the range stack provides an energy measurement which is used in photon vetoing, as well as tagging of the subsequent decays of muons and pions as discussed in section 3.2.2.

The range stack is a cylindrical shell of plastic scintillator surrounding the drift chamber and interior to the barrel veto. It is segmented into 24 azimuthal sectors and 21 radial layers. An enlargement of one of the sectors is shown in figure 4.7. The innermost layer, called a T-counter, having a shorter active length in the z–direction serves to restrict the angular acceptance to 2π. This is done to eliminate tracks which are oblique with respect to the detector midplane and may be the result of scattering off the drift chamber endplates or the steel support structure that protrudes part way into the stack.

There are two layers of multi-wire proportional chambers interleaved at two radii in the range stack to provide more accurate tracking which is used for offline corrections to the range.

Within each sector the 21 layers of scintillator are actually read out as 15. Because of spatial constraints at small radii the inner layers are optically coupled thus reducing the required number of phototubes. No significant loss in range resolution is caused by this arrangement since the tracks of interest have longer range.

Light is collected by phototubes at each end of the range stack and the the signals from these are processed as follows. Analog–to–digital converters integrate the pulse height for the energy measurement. Transient digitizers (500 MHz) record the pulse shapes for decay sequence identification, and discriminators provide fast signals for triggering. The cost of TD's prohibits

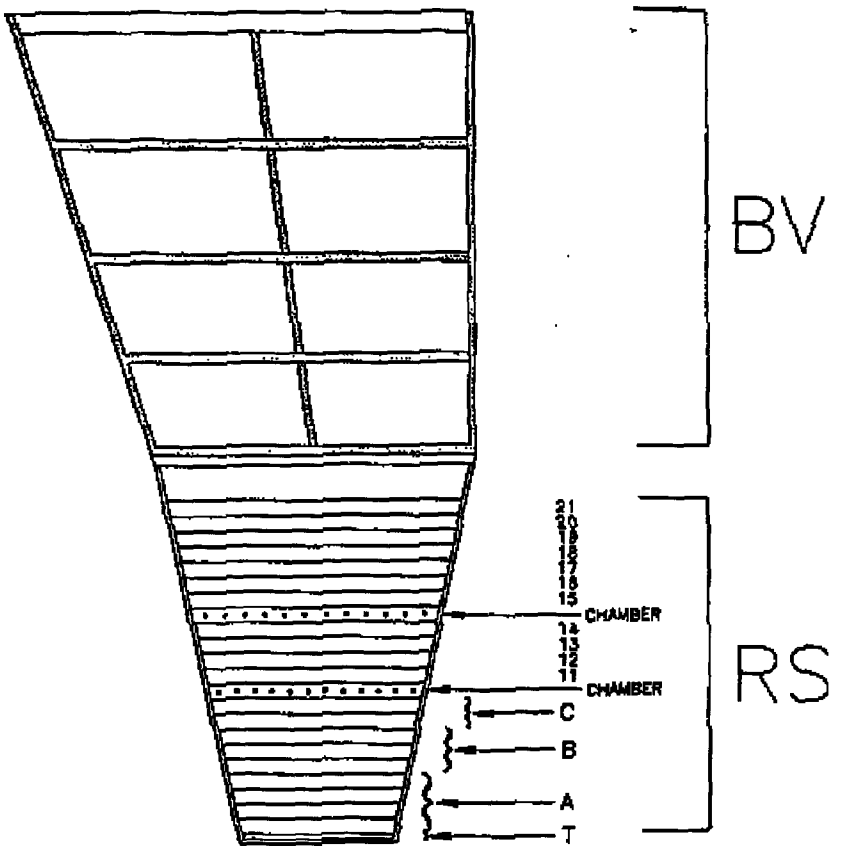

Figure 4.7: View of a sector of the range–stack

instrumentation of each PMT individually so at present every four PMT's are multiplexed to one TD channel.

4.8 The Photon Veto

The last line of photon detection is provided by a detector with many radiation lengths comprised of alternating sheets of 5mm scintillator and 1mm lead sheets. This combination is configured in the shape of a cylindrical shell, called the barrel veto (BV), placed outside the range stack, as well as in the shape of two discs, called the endcap veto (EC) which are parallel to and cover the drift chamber endplates. In this manner almost 4π solid angle coverage of photon detection is achieved.

The barrel veto is made up of counters arranged in 48 azimuthal sectors and 4 radial layers supported along their entire length by a stainless steel frame built into the interior of the magnet. In order to prevent photons escaping through the gaps between sectors these have all been placed skewed with respect to the radial direction so that none of the gaps point back to the target (see figure 4.7). A mixer block couples the scintillator sheets within a module whence light is brought out through the magnet end–plate by lucite light guides which feed a PMT sitting outside the magnet.

The endcap modules are composed of 24 azimuthal petals. The signal is collected by a compact fluorescent wave shifter bar placed on the outer radial face of each petal. Scintillation light from the petal excites the wave–shifter, and the light from the latter is brought out by light guides through the magnet endplate and feeds a PMT sitting outside.

Barrel and endcap veto elements are instrumented by ADC's and TDC's for precision offline analysis, as well as by summers for the purpose of forming fast analog total energy sums. These sums are discriminated and used for online vetoing of events containing photons. Although the online vetoing suffers from errors due to accidentals, it is instrumental in suppressing the $K_{\pi 2}$ background and reducing the number of events written to tape. A more precise veto, which takes energy deposited in other scintillating elements as well as timing into account, is

subsequently performed offline.

4.9 Upgrades

Between the 1990 and 1991 runs a few modifications to the detector were made. A $10cm$ portion of the BeO degrader at the downstream end was replaced with lead–glass read out with high–field phototubes thus making that part of the degrader active. Also, beam counters B3, B3S, and B4T were removed. Finally, a small single–layer cylindrical drift chamber, called the inner wire chamber (IWC), was placed in the air gap between the target and the main drift chamber.

There are a number of further upgrades to the detector, in addition to the UTC, being made for the next experimental run. A new beamline (LESBIII) has been constructed with an improved production target, two separators, and improved beam optics. This will result in an K^+/π^+ ratio of about 2, which represents a fourfold improvement over LESB I, as well as a twofold increase in K^+ flux. The beam counters have been modified to fit inside the smaller aperture of the UTC and an extra MWPC has been added. The number of x and y fingers in the B4 counter has been increased from 6 to 8, and the third layer B4T has been removed. In addition, B1 and B2 will be used for beam tuning but will be removed during actual running because they scatter kaons away from the target. A new target has been constructed with square fibers instead of round ones in order to minimize the amount of dead material between the scintillating fibers. The range–stack will have layers A,B, and C demultiplexed and straw–tube chambers will replace the range–stack MWPC's. At least one of the endcap photon vetoes, currently composed of lead–scintillator sandwich, will be replaced with pure CsI read out with high–field phototubes. Two sets of "collar detectors" (of lead–scintillator sandwich) will be added. One set will be placed between the endcap vetoes and the magnet steel at the upstream and downstream ends. A second narrower one will be placed at the downstream end to just surround the target between it and the magnet steel. This will be done to plug holes in the photon veto for photons escaping along a path almost parallel to the beam.

Chapter 5

The Ultra–Thin Drift Chamber

5.1 Introduction

The function of the drift chamber is to provide precise tracking of decay particles. The radius of curvature of the track in the magnetic field is used to make a precise determination of the decay particle momentum. Also, extrapolation of the particle trajectory out of the drift chamber volume back into the target and out into the range stack aids in pattern recognition for interpreting target element hits and allows for offline corrections to particle range based on the angle of entry into the scintillator. The new chamber has been designed to have as few radiation lengths as possible and, for this reason, is called the ultra-thin chamber or UTC.

The main reasons for the desirability of a low-mass or thin chamber are the following. Multiple Coulomb scattering of the particle in the chamber gas and in the wires decreases the momentum resolution of the chamber. Monte-Carlo calculations indicate that the current drift chamber's resolution is, in fact, limited by multiple Coulomb scattering and that a factor of 2 improvement in momentum resolution could be achieved by a factor of 5 reduction in the number of radiation lengths coupled with a 20% increase in size. This is what the UTC is designed to achieve and is the primary motivation for its construction. Also, it is desirable to reduce the amount of inactive material because short–range charged particles stopping in it will not be detected.

5.2 Physical Description

The UTC consists of 5 cylindrical concentric chambers. The first, third, and fifth are drift chambers containing axially strung sense and field-shaping wires and an Argon-Ethane gas mixture. These are called the first, second, and third superlayers respectively. The second and fourth chambers serve merely as spacer volumes and are filled with Helium gas. The chambers are separated from one another by copper clad Kapton foils which serve as cathode planes and as gas seals.

In what follows, a description of the composition of the chamber is given starting from the

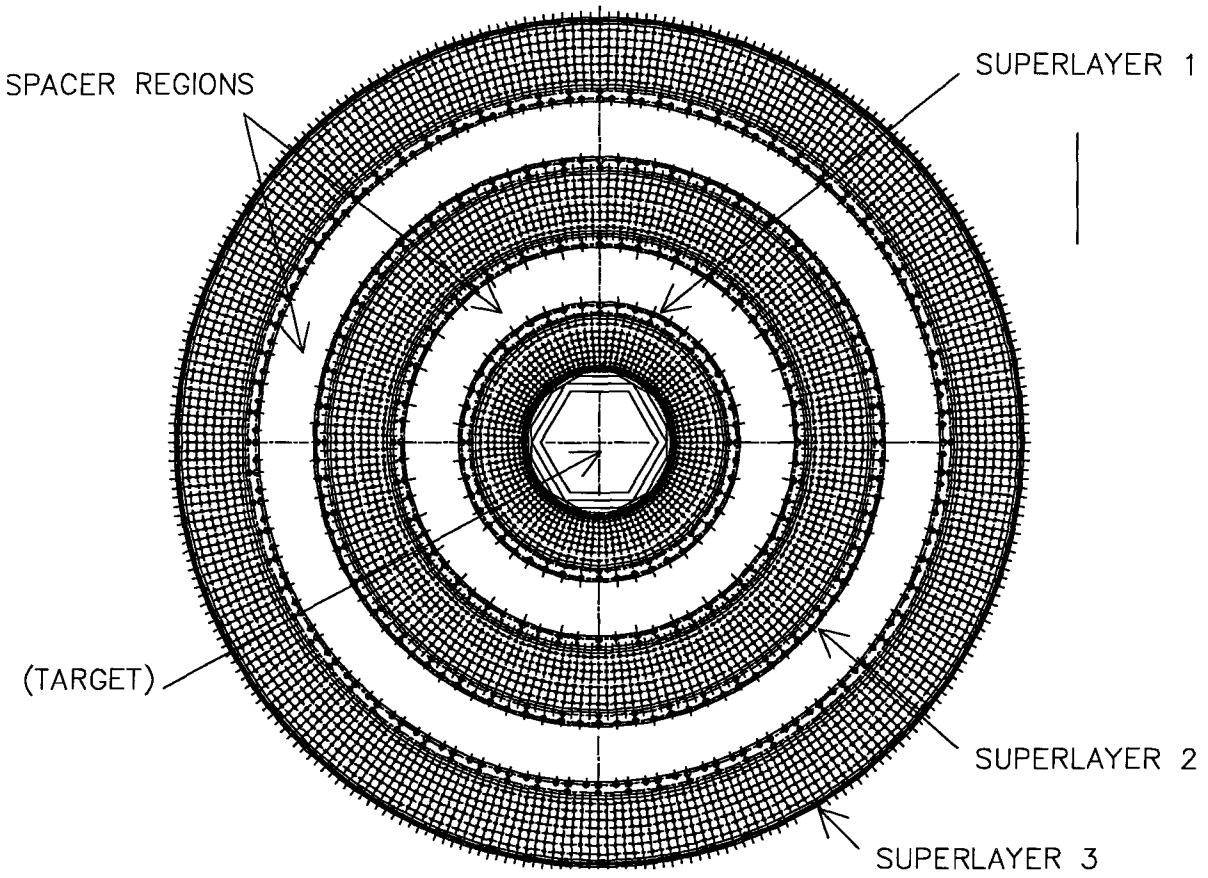

Figure 5.1: End View of UTC

inner radius and working outwards, and the reader is asked to refer to figures 5.1 and 5.2.

The innermost component is a cylinder made of G10 clad with copper which will be grounded in an effort to produce a quiet RF environment for the sense wires. It is this cylinder along with the outermost carbon-fibre cylinder which supports the load placed on the endplates by the tension in the wires. A cathode foil is glued onto the cylinder. The foil is made of a substance similar to mylar having the trademark name Kapton clad with strips of copper coated with nickel which run at an angle with respect to the axis of the cylinder. At one end of the chamber, the downstream end, the strips are glued onto copper pads on a plastic shim using conductive epoxy. Traces from these copper pads are soldered to inline connectors onto which are mounted the pre–amplifiers that read out the charge on the strips. Aside from the number

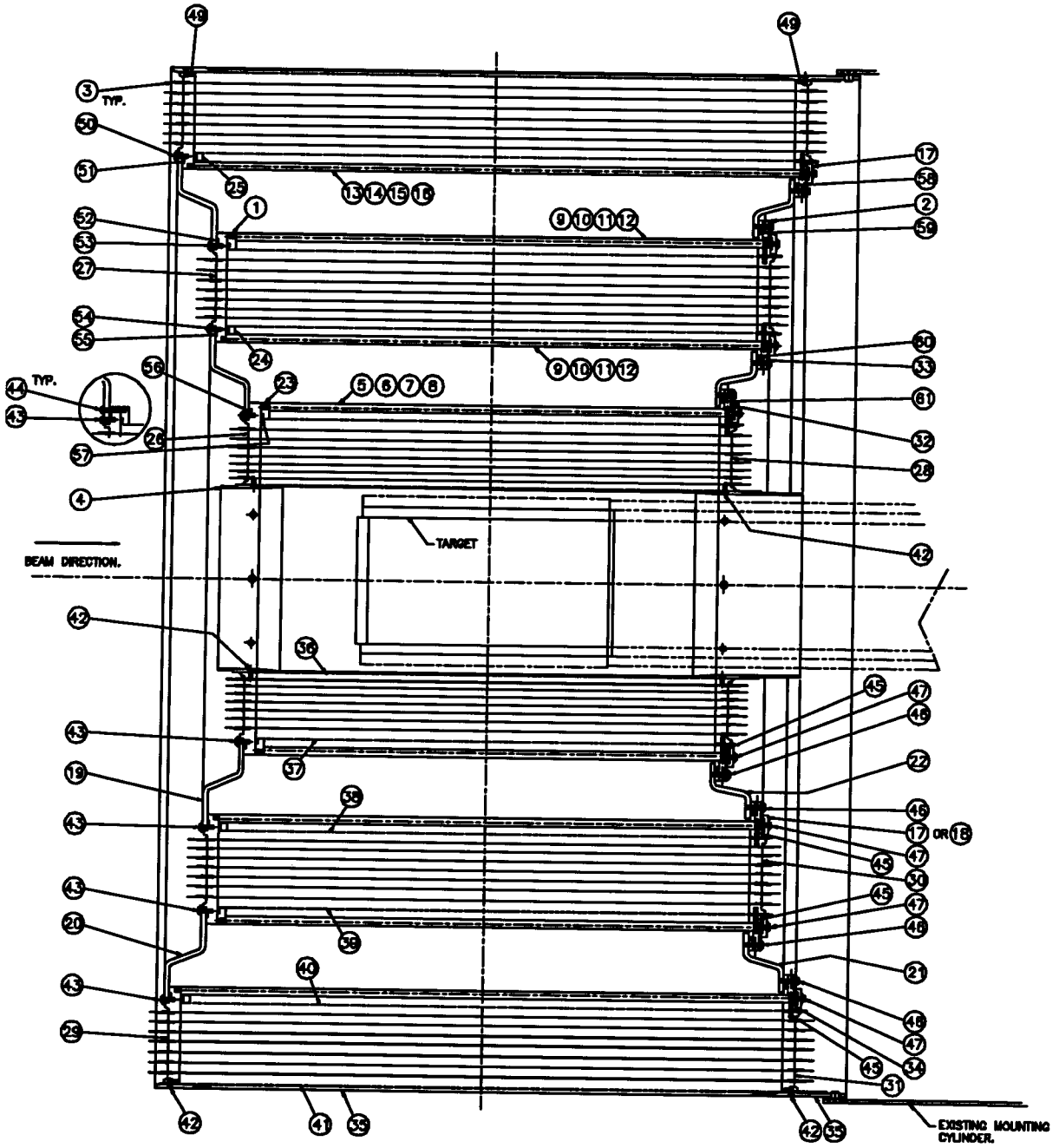

Figure 5.2: Side View of UTC

Table 5.1: Table of UTC components depicted in side view

Item	Description	Material	Qtem.
1	FOIL SUPPORT RING E–31014	NORYL 731	1
2	FOIL SUPPORT RING E–31015	NORYL 731	1
3	CRIMP PIN B–3914	Cu	8064
4	INNER TUBE ASS'Y D–33340	AL/G–10	1
5	EXPANSION SUPPORT ROD D–33350#1	AL.	6
6	COMPRESSION SUPPORT ROD D–33350#2	AL.	6
7	EXPANSION SUPPORT ROD D–33350#3	AL.	6
8	COMPRESSION SUPPORT ROD D–33350#4	AL.	6
9	EXPANSION SUPPORT ROD D–33350#5	AL.	20
10	COMPRESSION SUPPORT ROD D–33350#6	AL.	20
11	EXPANSION SUPPORT ROD D–33350#7	AL.	20
12	COMPRESSION SUPPORT ROD D–33350#8	AL.	20
13	EXPANSION SUPPORT ROD D–33350#9	AL.	18
14	COMPRESSION SUPPORT ROD D–33350#10	AL.	18
15	EXPANSION SUPPORT ROD D–33350#11	AL.	18
16	COMPRESSION SUPPORT ROD D–33350#12	AL.	18
17	COMP.ROD END PIECE D–33350#13	AL.	88
18	EXP. ROD END PIECE D–33350#14	ST.	88
19	SUPPORT RING D–33355	AL.	1
20	SUPPORT RING E–31033	AL.	1
21	SUPPORT RING E–31034	AL.	1
22	SUPPORT RING D–33356	AL.	1
23	FOIL SUPPORT RING D–33370	NORYL 731	1
24	FOIL SUPPORT RING E–31040	NORYL 731	1
25	FOIL SUPPORT RING E–31041	NORYL 731	1
26	WIRE SUPPORT RING D–33371	NORYL 731	1
27	WIRE SUPPORT RING E–31042	NORYL 731	1
28	WIRE SUPPORT RING D–33380	NORYL 731	1
29	WIRE SUPPORT RING E–31043	NORYL 731	1
30	WIRE SUPPORT RING E–31045	NORYL 731	1
31	WIRE SUPPORT RING E–31049	NORYL 731	1
32	FOIL SUPPORT RING D–33404	NORYL 731	1
33	FOIL SUPPORT RING D–33405	NORYL 731	1
34	FOIL SUPPORT RING E–31054	NORYL 731	1
35	OUTER TUBE ASS'Y E–31056	AL/C.F.	1
36	#1 FOIL CYLINDER	KAPTAN	1
37	#2 FOIL CYLINDER	KAPTAN	1
38	#3 FOIL CYLINDER	KAPTAN	1
39	#4 FOIL CYLINDER	KAPTAN	1
40	#5 FOIL CYLINDER	KAPTAN	1
41	#6 FOIL CYLINDER	KAPTAN	1
42	FLHDMACHSCR. #4–40 UNC X 3/8 LG.	SS	160
43	PANHDMACHSCR. #4–40 UNC X 5/16 LG.	SS	168
44	PANHDMACHSCR. #4–40 UNC X 3/4 LG.	SS	176
45	SKTHDMACHSCR. #4–40 UNC X 3/4"LG.	SS	176
46	PAN HDMACHSCR. #4–40 UNC X 5/8 LG.	SS	176
47	PANHDMACHSCR. #4–40 UNC X 1/2 LG.	SS	88
48	DOWELS B–30023	BRASS	32
49	O–RING 3/32 W DIA X 848 I.DIA.	BUNA–N	2
50	O–RING 3/32 W DIA. X 708 I.DIA	BUNA–N	1
51	" " " " 700 "	" "	1
52	" " " " 566 "	" "	1
53	" " " " 558 "	" "	1
54	" " " " 416 "	" "	1
55	" " " " 408 "	" "	1
56	" " " " 280 "	" "	1
57	" " " " 272 "	" "	1
58	" " " " 874 "	" "	1
59	" " " " 590 "	" "	1
60	" " " " 382 "	" "	1
61	" " " " 306 "	" "	1

of strips, radius, and length all of the cylindrical foils mentioned are similar. At either end of the support cylinder are glued two annular endplates made of a plastic having the trademark name Ultem[1]. These endplates have small holes drilled in concentric circle patterns or layers at seven different radii. These holes house gold-plated pins crimped around the cathode and sense wires which populate the drift region between the plates. The high-voltage distribution cards are attached to the pins on the upstream endplates, and the pre-amplifiers which read out the anode wires are attached to the pins on the downstream endplates.

There are two types of wires. The anode wires are 20 μm in diameter and are made of gold-plated tungsten. These are maintained at high voltage and are read out through fast analog preamplifiers. The cathode wires are 100 μm in diameter and made of gold-zinc plated aluminium. They are grounded and not read out. The anodes and cathodes are strung under a tension of 50g and 100g respectively. The wires are arranged in the seven layers as follows. The innermost layer is populated by both anode and cathode wires in an alternating pattern. The second layer is composed entirely of cathode wires, as are the fourth and the sixth. The third,fifth, and seventh layers are similar to the first.

However, the anode wire positioning between these layers is staggered so that an anode wire in any of these layers lines up radially with a cathode wire in the previous or next odd layer. Within a superlayer, there are the same number of wires in each layer, however, the number of wires varies between superlayers. Otherwise, the number of layers and the arrangement of anode and cathode wires is the same for all three superlayers. The number of anodes and cathodes in each wire layer as well as the number of strips on each foil are summarized in table 5.2.

Surrounding the first superlayer is a cathode strip foil (foil 2). At the downstream end there is an additional G10[2] ring screwed and glued to the wire endplate. The foil is mounted on the inside of a Noryl[3] ring which is pushed up against the G10 ring and fastened with screws. An O-ring is used to provide a gas seal between the Noryl and G10 rings. At the upstream end

[1] Ultem is a registered trademark of General Electric
[2] G10 is a trade name for an insulating glass–epoxy composite
[3] Noryl, a machinable plastic, is a registered trademark of General Electric

Table 5.2: Table of UTC Electrode Layers

LAYER	SUPER–LAYER	TYPE	RADIUS [cm]	ANODE WIRES	CATHODE WIRES	CATHODE STRIPS
1	1	Foil	80.00	–	–	48
2	1	A or C	85.60	48	48	–
3	1	C or C	91.20	0	96	–
4	1	C or A	97.59	48	48	–
5	1	C or C	103.98	0	96	–
6	1	A or C	111.26	48	48	–
7	1	C or C	118.54	0	96	–
8	1	C or A	126.84	48	48	–
9	1	Foil	135.14	–	–	72
10	2	Foil	214.00	–	–	108
11	2	A or C	221.24	96	96	–
12	2	C or C	228.48	0	192	–
13	2	C or A	236.21	96	96	–
14	2	C or C	243.94	0	192	–
15	2	A or C	252.19	96	96	–
16	2	C or C	260.44	0	192	–
17	2	C or A	269.25	96	96	–
18	2	Foil	278.06	–	–	144
19	3	Foil	359.58	–	–	180
20	3	A or C	367.46	144	144	–
21	3	C or C	375.48	0	218	–
22	3	C or A	383.86	144	144	–
23	3	C or C	392.22	0	218	–
24	3	A or C	400.72	144	144	–
25	3	C or C	409.72	0	218	–
26	3	C or A	418.86	144	144	–
27	3	Foil	428.00	–	–	216

the foil is glued directly to the wire endplate. Aluminium flanges attached to the G10 extender ring at the downstream end, and to the endplate at the upstream end, extend the next sections of the chamber out in the axial direction as well as providing spacing in the radial direction. This is done to maintain the solid angle covered by the detector. Another cathode foil is glued onto the outer edges of two Noryl rings. At the downstream end the ring partially overlaps the aluminium flange and is fixed to it by screws. At the upstream end the overlap is complete and once again, screws are used to fix the Noryl ring to the aluminium flanges. At both ends an O–ring seal is made between the aluminium flange and the Noryl ring.

Two more endplates, this time made of Noryl, surround foil 3. At the downstream end, the endplate is fastened to the foil ring with radial screws. At the upstream end, the endplate is supported by the aluminium flange to which it is fixed by axial screws. The second superlayer is strung similarly to the first and is surrounded by another cathode foil (foil 4). This foil is glued to a Noryl ring which seals up against another aluminium extender flange screwed directly to the upstream endplate of superlayer 2. At the downstream end, the foil is glued to the outside edge of the downstream endplate. The connector shim is epoxied to it and another Noryl extender ring fastened to the endplate with radial screws. To this is fastened another aluminium flange. From here the inner foil for superlayer three (foil 5), the foil rings and endplates are assembled as for superlayer two. The outer foil for superlayer 3 (foil 6) will be glued onto a carbon-fibre cylinder padded with ROH–A–CELL, a styrofoam-like substance. The carbon–fibre cylinder will be fixed to it with radial screws.

5.3 Thickness of the UTC

The amount of material in the chamber is important for two reasons. Firstly, multiple scattering in the tracking volume itself will cause the tracks to deviate from the ideal circular paths, resulting in larger experimental errors on the radius of the circle fit. This is discussed more quantitatively in section 5.6 below. For these purposes one need only consider the material through which the particle must pass once it has entered the tracking volume. That is, one

Table 5.3: Breakdown of radiation lengths in tracking volume of old drift chamber

COMPONENT	NO. OF RAD. LENGTHS
Argon–Ethane gas	2.0×10^{-3}
wires	6.4×10^{-3}
TOTAL	8.4×10^{-3}

Table 5.4: Breakdown of radiation lengths in tracking volume of the UTC

COMPONENT	NO. OF RAD. LENGTHS
foils 2,3,4,5	0.37×10^{-3}
Argon–Ethane gas	1.05×10^{-3}
Helium gas	0.03×10^{-3}
wires	0.20×10^{-3}
TOTAL	1.65×10^{-3}

may ignore the inner and outer support tubes as well as the innermost and outermost foils. The number of radiation lengths of the various components as well as the total number of radiation lengths in the tracking region have been calculated for the old drift chamber [24] as well as for the UTC. They are presented in tables 5.3 and 5.4 below. They have been calculated for a trajectory proceeding radially outward in a plane transverse to the cylindrical axis of the respective chambers.

The scattering in the inner support tube will not affect the circularity of the track and so will not reduce the quality of the fit but it will, of course, alter the trajectory of the particle before it enters the chamber. The outer support tube simply comprises more dead material through which the particle must pass before entering the range–stack. The breakdown of the radiation lengths for the whole chamber is presented in table 5.5.

5.4 Operation of the UTC

The arrangement of anode and cathode wires and cathode foils described above results in the establishment of roughly square drift cells which may be thought of as individual proportional counters. Physically, each cell is centred on an anode wire and defined by the square formed

Table 5.5: Breakdown of radiation lengths in entire UTC

COMPONENT	NO. OF RAD. LENGTHS
foils 1 and 6	0.19×10^{-3}
inner gnd plane	1.18×10^{-3}
inner support tube	0.20×10^{-3}
outer support tube	2.55×10^{-2}
tracking region	1.65×10^{-3}
TOTAL	2.87×10^{-2}

by linking its neighbouring cathode wires, or its neighboring cathode wires and adjacent foil.

As previously mentioned, the anode wire is held at high potential thus creating an electric field emanating from the wire. When a charged particle passes through the drift–cell region it ionizes the gas, and electrons from the ionization drift toward the anode wire. When they come to within a few wire diameters of the anode they undergo significant acceleration and obtain sufficient kinetic energy to ionize the gas themselves. Both the original and newly liberated electrons are again accelerated and cause further ionization. This process is repeated until all the electrons reach the surface of the anode wire and are captured. In this manner, and with sufficiently high electric fields, electron multiplication factors of up to 10^5 can be attained. The positively charged ions drift toward the cathode wires and foil strips. However, current pulses occur on the cathode strips due primarily to the charge induced by the anodes. The current pulses or induced charges are read out and enhanced by electronic amplifiers connected to the anode wires and cathode strips.

Since there is no electric field component applied in the axial, or z, direction, the liberated electrons, do not drift axially. Thus the avalanche on the wire will be localized in the z direction. This localized electron swarm induces charge on the nearby cathode foil strips, with cathode strips nearer the avalanche having larger induced charge than those further away. Since the cathode strips run at an angle with respect to the wires, the intersection of the wire and cathode strip defines a range in z with some central value. By taking an average of these central z values of hit strips weighted by the relative induced charges one can infer the z coordinate of

the trajectory of the charged particle which gave rise to the ionization.

The time of passage of the particle through a given drift cell can be estimated from hits in the I and V counters mentioned in section 4.5. Given the speed of the charged particles and the distances involved, the delay between entering the UTC and passing through any given cell is presumed to be insignificant. Measuring the time of onset of the anode current pulse with respect to the estimated time of the passage of the particle through the cell permits estimation of the radial distance from the anode of the point of closest approach of the particle trajectory. This estimate translates into contours about the anode wires to which the trajectory must have been tangent. To the degree that the electric field is purely radial in direction and isotropic with respect to the x and y coordinates, these contours will approximate circles. However, the relationship between wire hit times and drift distances in various directions can be calculated in detail based on electric field, gas pressure and gas characteristics. In practice they are calibrated based on a set of test data with a uniform spread of particle trajectories over the volumes of the drift cells.

Given the speed of the particles the drift chamber seeks to track, it is assumed that the predominant interaction they undergo is with the axial magnetic field. This leads to a helical trajectory, whose projection is a circle in the x–y plane. Therefore, the particle trajectory is inferred by fitting the best circle which is tangent to the above calculated contours. The pitch of the helix is derived from the z measurements from the cathode foils.

5.5 Comments on Design

5.5.1 Mechanical

The chamber consists of many pieces and is quite complex mechanically. Aside from the labour involved in assembly, the drawback to such a design is the problems it presents in obtaining precision alignment of its various components. Fortunately, alignment between superlayers does not affect the resolution and so these translational and rotational offsets from an ideal, cylindrically symmetric chamber system can be calibrated out. The justification for this design

is that it renders the entire chamber accessible for the purposes of maintenance. Indeed, the various superlayers can be removed individually, have their foils replaced, and be entirely or partially restrung. It was originally planned to have the foils glued to their support rings which would then be screwed in place. However, for purposes of providing good gas seals they were glued to the endplates. Nevertheless, experience has shown that it is still possible to remove them without damaging the superlayer.

The foil material was chosen to be Kapton primarily due to its low leak rate for He gas. Leakage of the Helium gas from the spacer volume into the drift–cell superlayers would reduce the gas gain. The use of 2cm of water equivalent pressure differential from the interior to exterior volume of each foil combined with a 40g/cm tension has been calculated to maintain the cylindrical shape of the foil to within 1mm [12]. According to field calculations of the drift cell, a uniform field can be achieved with a 1mm tolerance between the anode and the cathode foil. The tensions on the wires are to prevent deformation due to electrostatic and gravitational forces. The sense wires are tensioned at 50g and the cathodes at 100g for a total load on the endplates of 300kg. This is much less than the 880kg loading of the old drift chamber allowing thinner and lighter endplates to be used.

The choice of Noryl was made for the endplates and foil rings in order to reduce the radiation lengths in the chamber. It is a low–density plastic with good dimensional stability and is relatively easy to machine. It is also a good insulator and thereby at once resolves the problem of isolating the anode pins protruding from the endplates. On the other hand, a grounded aluminium endplate would have produced extra shielding against RF noise. Previous experience with Noryl had confirmed its good dimensional stability, however, this experience had been for relatively small pieces. With the UTC some problems with creeping and warping of the larger endplates have tended to hinder efforts at aligning and positioning them properly.

5.5.2 The Drift Gas

The drift gas used is an argon (49.9%), ethane (49.9%), ethanol (0.2%) mixture. The reasons for this choice are the ability to operate at high gas gain, the reasonably fast drift velocity, and the saturation of the drift velocity (explained below).

Avalanche multiplication occurs in noble gases at much lower fields than in complex molecules. This is due to the fact that the latter have many non-ionizing modes of energy dissipation. The choice of argon from among the noble gases arises from the high specific ionization coefficient. This is the average number of ions produced by a minimum–ionizing particle. The specific ionization coefficient of argon is exceeded only by those of xenon and krypton which are ruled out by their expense.

A chamber filled solely with pure argon cannot operate at gas gains higher than 10^3 or 10^4 for the following reasons. During avalanche excited and ionized atoms are produced. An excited noble gas atom can only dispose of its energy and return to the ground state by emitting a photon. For argon the minimum energy of such a photon is $11.6eV$ which is greater than the ionization potential of any metal used in the cathodes. Thus, photoelectrons are extracted from the cathode which, in turn, avalanche causing spurious signals. Also, the ionized argon atoms migrate to the cathode where they are neutralized. The energy released from the electron capture is either radiated as a photon or by the ejection of another electron from the cathode metal. Both of these lead eventually to another spurious avalanche. Furthermore, the probability of these events is great enough as to result in permanent discharge even for moderate gains.

Polyatomic molecules, on the other hand, especially those composed of greater than four atoms, have many non-radiative excited states (rotational and vibrational). They can thus absorb photons emitted from argon ions and dissipate the energy through elastic collisions or dissociation into simpler radicals. This is the role of ethane in the gas mixture; it is said to be a polyatomic quencher. In addition, when ionized polyatomic molecules neutralize at the cathode secondary emission is highly unlikely; they either recombine into simpler molecules or form larger complexes (polymerization).

For this reason, polyatomic quenchers, used as the sole additive, are detrimental to the lifetime of the chamber. This is because the created polymers deposit on the anode and cathode forming an insulating layer. Positive ions created from further avalanches continue to drift to the cathodes, settle on the the polymer surface and slowly diffuse through. Eventually, the positive ions build up on the surface of the polymer due to the excess of the rate of ionization over that of neutralization. Thus, a strong dipole electric field is created which extracts electrons from the cathode and sets off a permanent discharge. This is known as the Malter effect.

In order to avoid this problem it is possible to make use of quenchers which do not polymerize. These are substances such as alcohols, aldehydes, and acetates. The problem with these, however, is that their vapor pressure is low compared to that of hydrocarbons. As a result their overall efficiency in quenching against photoionization and secondary emission when mixed in with the drift gas is also low.

Nevertheless, these non-polymerizing quenchers are used in the following manner to great advantage. By choosing a non-polymerizing agent with an ionization potential lower than the other components in the gas mixture, which includes a polymerizing hydrocarbon quencher for efficiency, use is made of an efficient charge exchange mechanism whereby the excess electrons are transferred from one species to the other such that all ions are removed except the one with the lowest ionization potential. Thus the ions arriving at the cathodes will be of the non-polymerizing type. This is the role of the ethanol in the gas mixture. This combination allows operation of the chamber reliably at a gas gain of about 8×10^4.

Finally, another desirable characteristic of this gas is that its drift velocity "saturates". That is to say that above a certain value of reduced field, the drift velocity of the gas is roughly constant. Reduced field refers to the ratio E/P, where E is electric field in V/cm and P is gas pressure in *torr*. The relationship between drift velocity and E/P, as calculated by GARFIELD, a program for modelling multi-wire chambers, E/P, is depicted in figure 5.3.

It is seen that at the upper values of E/P, such as 340 $kV/cm \cdot torr$ at which the UTC operates, the drift velocity does not vary much. Note that the plot is logarithmic in the reduced

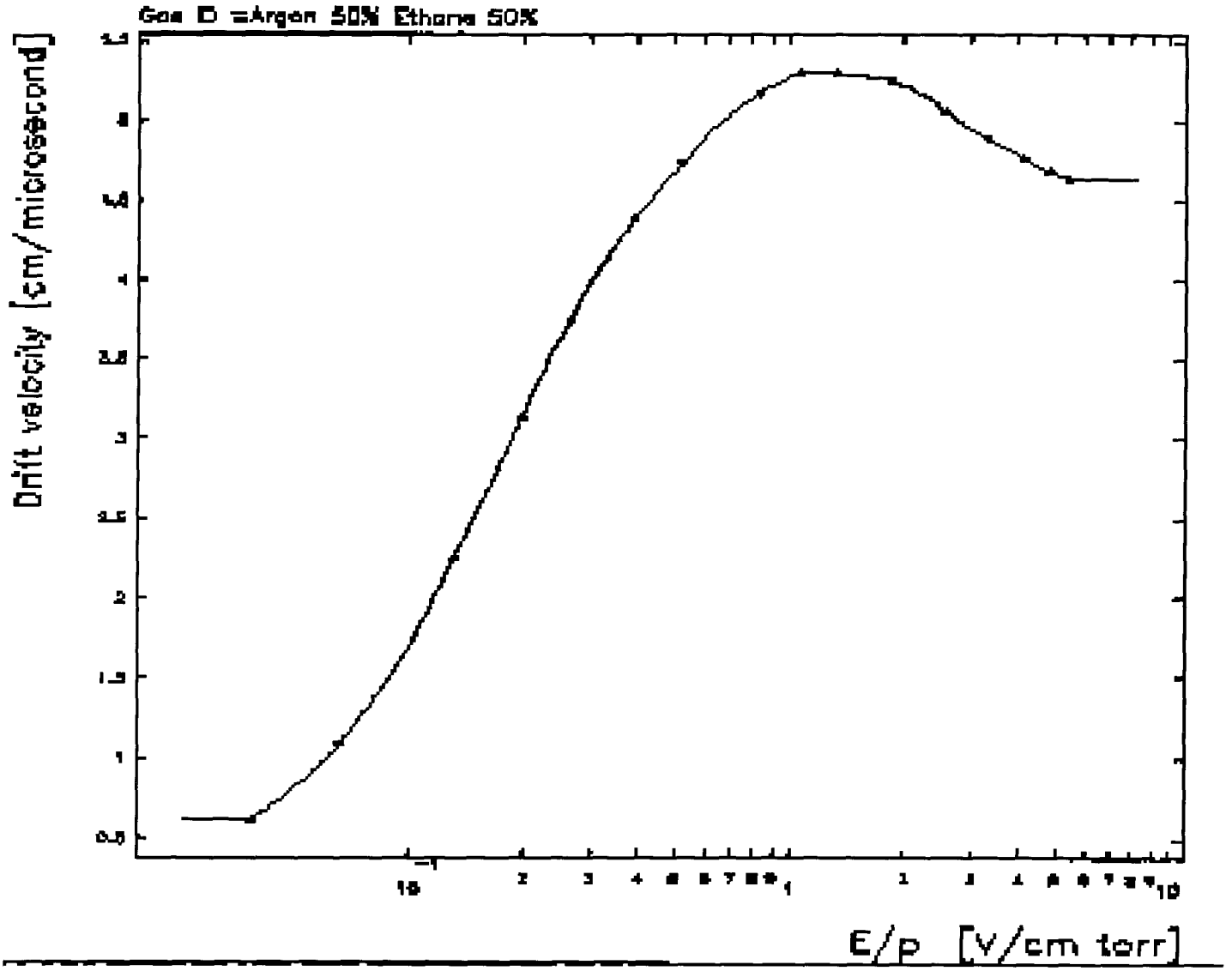

Figure 5.3: Drift Velocity vs Reduced Field for 50%–50% Ar–Ethane

field. In calculation of drift distances from the times of the pulses a constant drift velocity is not assumed, but rather a space-time relation is inferred from calibration data taken at intervals assuming a uniform distribution of ionizing tracks. This takes into account non-uniformity in the electric field but still assumes that the drift properties of the gas are constant over time. Since the electric field at each point in the drift cell is due to the well controlled potentials on the wires the only remaining variable is pressure. Therefore, the saturation of the gas insures that the space-time relations do not depend strongly on the pressure. This avoids the need for close monitoring and control, in absolute terms, of the pressure in the drift chamber.

The use of helium in the spacer regions between superlayers is obvious. It is a light—in order to reduce multiple scattering—non-flammable gas used to blow out and shape the foils.

5.5.3 Drift Cells

The layout of the wires leads to drift cells which are physically adjacent, non-overlapping, and roughly square in shape. Its shape leads to a field which is approximated well over a large area of the drift cell by the field due to an infinitely long cylindrical shell of charge. The latter has the following cylindrically symmetric form:

$$E(r) = \frac{V}{r \ln b/a} \tag{5.1}$$

where a is the radius of the anode and b is some average radius to the edges of the cell which are at almost zero potential. It follows that the isochrones, or contours of equal drift time from the wire, will be roughly circular. The values of potential to be applied to the anodes were calculated subject to the following constraints. The field on the surface of the anodes is kept at or below $260 kV/cm$ in order to prevent spontaneous field emission around the anodes. This is still on the conservative side. Also, the surface field on the cathodes is kept below $30 kV/cm$ in order to prevent "whisker growth", the polymerization of trace impurities in the gas onto the cathodes. The calculation was done using GARFIELD. It was not assumed that cells in the same layer or superlayer were perfectly isolated from one another. Thus, the potentials for an

entire superlayer were optimized together and different values of potential were found for each layer. These are summarized in table 5.5.3 below.

As can be seen, none of the anode wire surface fields exceed $260kV/cm$, in fact, they are backed off somewhat from that value. The surface fields at the cathodes are nowhere near $30kV/cm$ so it can be seen that the anode surface fields are the limiting factor.

5.6 The Momentum Resolution

The momentum resolution of the UTC was studied prior to its construction in two different ways. The first way was by a Monte–Carlo study which used a specialized program, called UMC, based on the EGS package, which can generate events and model their effect on all the components of the detector to produce data that can be subsequently analyzed by the analysis package, KOFIA [13]. The measure of resolution used was $\Delta P = P_{meas} - P_{true}$ of the particles in the drift chamber.

The momentum derived from equally spaced measurements of a charged track in the $x - y$ plane, transverse to the magnetic field, is given by

$$P_{xy} = 0.3 \frac{MeV/c}{kG \cdot cm} qBR \tag{5.2}$$

where q is the charge in units of the electron charge, B is the magnetic field and R is the radius of curvature of the track. Neglecting non–uniformities in the magnetic field, the error in the momentum arises from errors in obtaining the radius of curvature of the track, or equivalently its inverse, k, called the curvature. The curvature error is due to two components, δk_{pos}, the error in measuring points on the track, and δk_{ms} the error due to deviation of the particle trajectory due to multiple scattering. These are given by

$$\delta k_{pos} = \frac{\sigma_{xy}}{L^2} \sqrt{\frac{720}{N+5}} \tag{5.3}$$

$$\delta k_{ms} = \frac{16 MeV/c}{L P_{xy} \beta} \sqrt{f} \tag{5.4}$$

where σ_{xy} is the $x - y$ measurement uncertainty of the wires, L is the path length of track, N

Table 5.6: Table of Optimized Potentials and Resultant Electrode Surface Fields

LAYER	SUPER–LAYER	ANODES		CATHODES	
		APPLIED POTENTIAL [kV]	SURFACE FIELD [kV/cm]	SURFACE FIELD [kV/cm]	
1	1	–	–	.9	
2	1	1.807	259.4	13.4	–
3	1	–	–	15.1	15.3
4	1	1.947	259.6	–	17.7
5	1	–	–	16.6	16.3
6	1	1.988	259.5	17.5	–
7	1	–	–	14.7	15.0
8	1	1.914	259.4	12.4	–
9	1	–	–	.6	
10	2	–	–	.7	
11	2	1.881	259.2	12.9	–
12	2	–	–	14.9	15.0
13	2	2.010	259.6	–	17.6
14	2	–	–	16.5	16.3
15	2	2.030	259.3	17.5	–
16	2	–	–	14.8	15.0
17	2	1.935	259.3	–	12.5
18	2	–	–	.6	
19	3	–	–	.7	
20	3	1.907	259.2	12.6	–
21	3	–	–	14.9	14.9
22	3	2.034	259.0	–	17.5
23	3	–	–	16.5	16.6
24	3	2.053	259.5	17.5	–
25	3	–	–	14.7	14.8
26	3	1.945	259.4	–	12.4
27	3	–	–	.6	

is the total number of measurements, f is the number of radiation lengths traversed, and β is the speed of the particle in units of the speed of light.

Propagating these errors through one obtains the following contributions to the momentum errors.

$$\left(\frac{\delta P_{xy}}{P_{xy}}\right)_{ms} = \frac{16MeV/c}{LqB\beta}\frac{\sqrt{f}}{0.3} \tag{5.5}$$

$$\left(\frac{\delta P_{xy}}{P_{xy}}\right)_{pos} = \frac{\sigma_{xy}P_{xy}}{0.3BL^2}\sqrt{\frac{720}{N+5}} \tag{5.6}$$

An average value of $f = 1.65 \times 10^{-3}$ has been estimated by looking at the various materials traversed by the particle. Putting $B = 10kG$, $L = 0.43m$, $\beta = 0.82$, and $P = 185MeV/c$ for $K_{\pi 2}$ pions in the chamber a value of $\frac{\delta P}{P} = 1.24MeV$ is obtained. This amounts to the bulk of the value obtained from the Monte–Carlo. Consideration of the position resolution contribution to the momentum uncertainty, leads to an improvement by a factor of 0.64 due to the increased track length measured by the UTC (36.3 cm instead of 29.0 cm).

The total momentum resolution as measured at the drift chamber is worsened by target contributions. When these were included in the Monte–Carlo a value of 2.3 MeV/c was obtained.

The second way in which the momentum resolution was studied was by actual construction of a prototype chamber by the Princeton group [14]. This chamber resembles the actual UTC except that it comprises only a sector of a cylinder and so does not cover the same solid angle and has fewer wires. Also, the cathode foil strips for the prototype chamber run at 90° to the wires whereas they run at roughly 45° to the wires in the UTC. The chamber was installed in the detector, a run was made and the results analysed using code written for the UTC. The momentum resolution obtained on the Princeton prototype chamber was 2.42 MeV/c.

The motivation for the construction of the UTC was primarily to increase the kinematic background rejection by improving the momentum resolution (roughly from 2% to 1%). Figure 5.4 depicts the sought and principal background spectra smeared with a Gaussian to account for the 2% resolution of the current chamber. Figure 5.5 depicts the same spectra smeared for 1% resolution corresponding to the UTC.

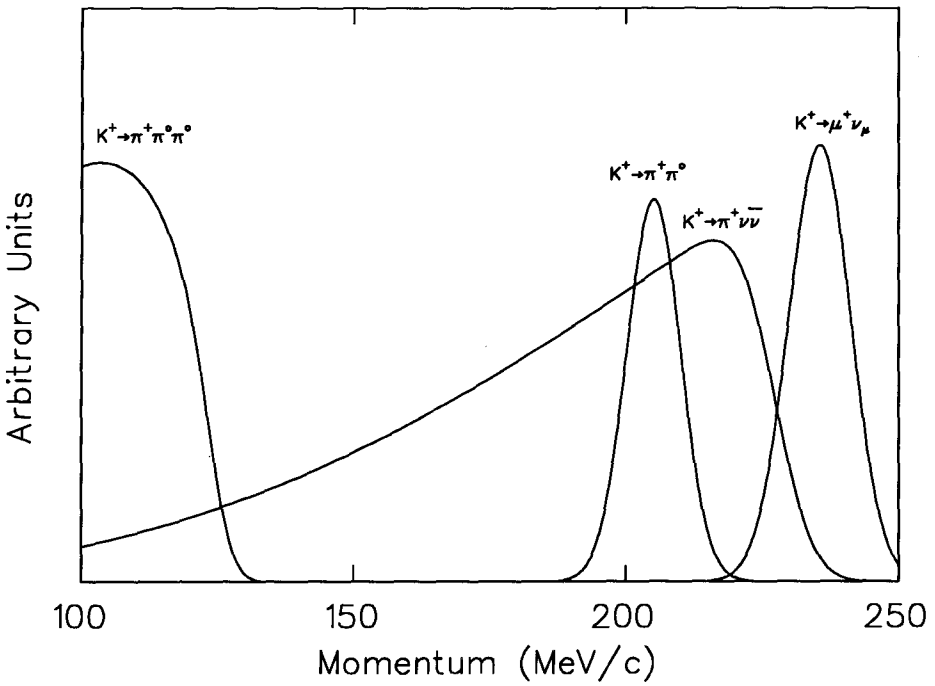

Figure 5.4: Momentum spectra with 2% resolution

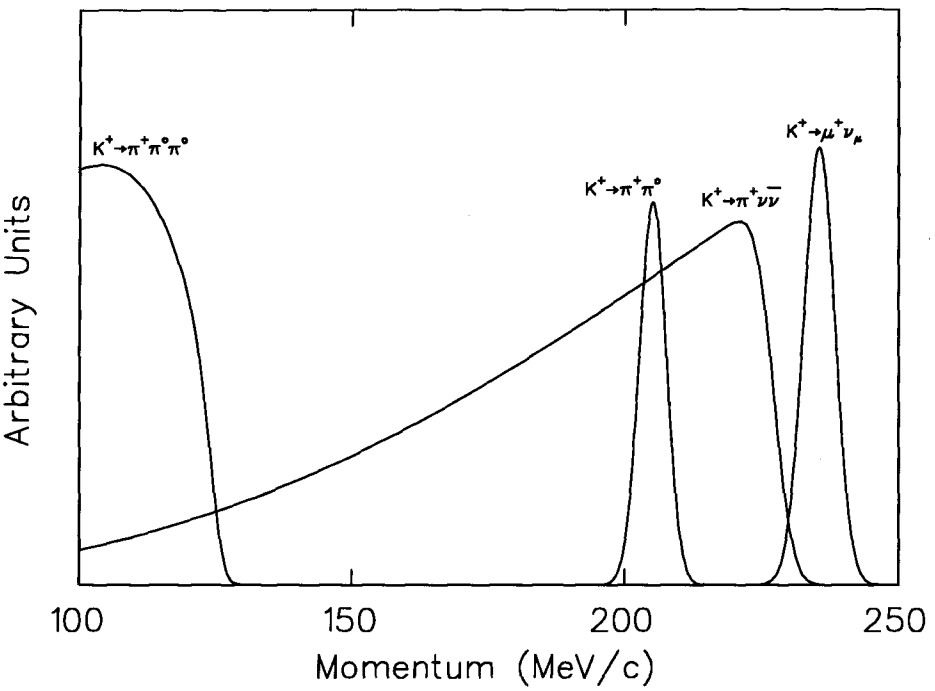

Figure 5.5: Momentum spectra with 1% resolution

It should be noted that the overlap between the $K_{\mu 2}$ spectrum and the $K^+ \rightarrow \pi^+ \nu\overline{\nu}$ spectrum is reduced significantly. For the purposes of background rejection the separation of the range spectra of $K_{\mu 2}$ and $K^+ \rightarrow \pi^+ \nu\overline{\nu}$ is much greater. Thus it is possible to eliminate essentially all the $K_{\mu 2}$ background by making cuts solely on the basis of range. Nevertheless, the improvement in momentum resolution will allow the momentum cut to be tightened adding further redundancy while still increasing the acceptance.

Chapter 6

The Read–Out Electronics

6.1 Introduction

The hits on wires and cathode strips caused by a charged track appear as current pulses or charge deposits on the electrodes in the chamber. These must be converted into analog and digital signals which then drive ADC's and TDC's. This is implemented in two stages, pre–amplifiers and post–amplifiers.

Post–amplifiers take analog signals from the pre–amps and perform some further amplification and pulse–shaping to produce an analog signal which is fed into the ADC's. They additionally provide discriminated signals which drive the TDC's.

Preamplifier cards are mounted directly onto the anode pins on the downstream endplate and onto connector pins soldered to the copper pads on the shims surrounding the foils, which make electrical contact with the strip through conductive epoxy. It is the task of these pre–amplifiers to convert the current or charge into voltage signals which are propagated down long cables to the postamplifiers located away from the detector. As a result, the design of the pre–amplifiers must take into consideration the inherent electrical characteristics of the electrodes and chamber, and it is their design which is discussed in this chapter.

6.2 Anode Pre–amplifiers

6.2.1 Description

The pre–amplifiers that will be used to read out the anode wires will be the same as for the old drift–chamber. A schematic diagram is given in figure 6.1. It is a discrete–design feedback amplifier based on the BFT25 transistor manufactured by Motorola. It is composed of four classic transistor amplifier stages. The first stage is a common–base current buffer which serves as a low impedance input. The importance of this is discussed below. The next three stages provide the open loop gain for the feedback amplifier. The second and fourth transistor (from the left of the figure) are used as buffers for the purposes of impedance matching. They serve to isolate the third transistor which used in the common–emitter configuration and provides

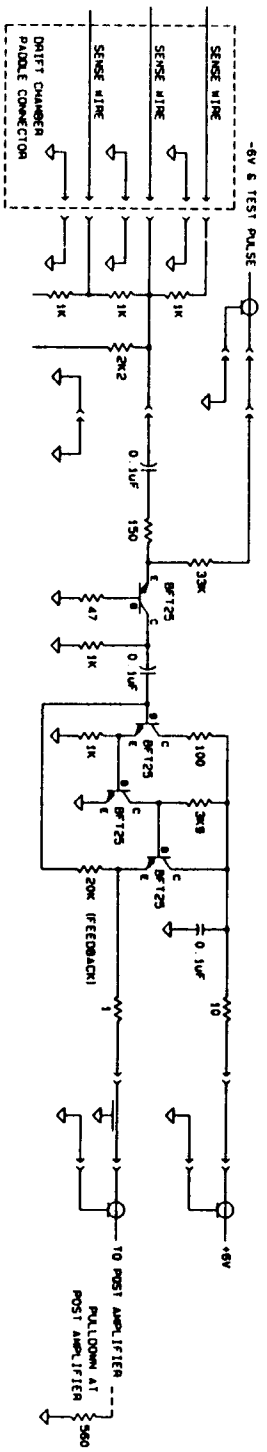

Figure 6.1: Anode pre-amplifier circuit diagram

most of the voltage gain. The entire circuit may be thought of as a current–to-voltage amplifier with a typical gain of $10mV/\mu A$.

6.2.2 Design Comments

The origin of the signal on the anode wire is due to the measurement of a charge in a system of total capacitance between anode and cathode of C, which given by [16]:

$$dV = \frac{Q}{CV_0}\frac{dV}{dr}dr. \tag{6.1}$$

where Q is the charge, V_0 is the potential between anode and cathode, r is the distance from the anode, and V is the potential at that distance.

Since the ions are generated near the anode and drift all the way to the cathodes their contribution to the induced signal is dominant at later times. Thus, if the anode were electrically isolated the voltage at the anode would increase as more and more ions drifted to the cathodes, until such time as all the ions had reached the cathodes. When the anode is read out, a differentiator is formed of time constant RC, where R is the input impedance of the amplifier (and C is still the inherent capacitance between anode and ground). To the degree that R can be made small, the differentiator becomes ideal, and short, sharp pulses are obtained. A shorter time constant does yield a signal with a lower peak value but the effect is minimal since the time growth of the voltage induced at the anode is very fast at the beginning, reaching half its final value in one–thousandth of the total time. Furthermore, since very little analog information from the anode pulse heights is used, the improvement of rate capability of the chamber outweighs the slight loss of pulse height. Such is not the case for the cathode strips as will be seen below.

6.3 Cathode Pre-amplifiers

The tracking of the z–coordinate of the particle is achieved with the cathode strips in the following manner. Clusters of cathode strips are first sought out. Then, for each hit strip,

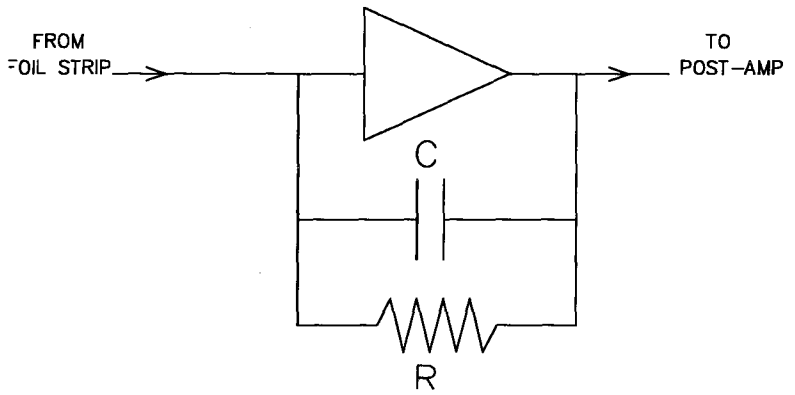

Figure 6.2: Schematic/Block Diagram of Charge Amplifier

the intersection is found between it and a wire hit which was roughly coincident with the hit on the strip. The intersection between the strip and such a wire yields a z–coordinate. These z–coordinates are weighted by the charge read out from their corresponding strips and averaged over the strips in the cluster to produce a centre of gravity for the charge which is taken to be the z–position of that portion of the track. Thus, the z–coordinate resolution of the chamber is dependent upon good signal to noise ratios for the cathode strip pulses read out. Timing considerations cannot be neglected altogether, since rate and coincidence with wire hits are still important. However, pulse height, in contrast with the situation for anodes, is of greater importance.

For this reason, the anode amplifiers described above are not optimal in this situation. Rather, what is required is a charge amplifier of the form depicted in figure 6.2.

This can be thought of as a current integrator, with integration time RC, or equivalently as a charge amplifier with gain $1/C$. The idea is to have the output remain significant over a large portion of the total ion drift time thereby collecting a larger signal, or charge, over the gate time of the ADC.

At present, an improvement in gain for the the foil strip read-outs on the inner two foils is crucial for the following reason. Due to the chamber geometry, the foil strips themselves have a capacitative coupling to the ground plane on the inner support tube. At the high frequencies of

these induced pulses the coupling acts to short out these signals thereby reducing the input to the (present anode) amplifiers and hence the overall gain. This effect is particularly pronounced for the first two foils as would be expected from the geometry and the measured strip–to–ground plane capacitances.

To compensate for this, high gain must be achieved by the read–out amplifiers themselves. In order not to exacerbate the problem mentioned above, the basic amplifier in figure 6.2 must have low input capacitance and be fast enough to cope with the high–speed signals involved.

An implementation of such a charge amplifier which was prototyped is presented in figure 6.3 below. The design is based on the NE253 series Gallium–Arsenide dual–gate MESFET. Referring to figure 6.3, the top MESFET, Q1, is configured as a constant–current source for biasing and provides a high signal impedance to the drain of the second MESFET, Q2, which is used as common–source amplifier. The choice of the NE253 is motivated by the fact that when the second gate terminal, G2, is grounded the input capacitance at G1 is reduced to a fraction of the a picofarad despite the high gain between the gate and drain. It does not suffer from the Miller effect. The common–source amplifier stage is followed by two buffers, BFT92 BJT's (Motorola) which serve to isolate the feedback path and the output. It should be noted that there is no actual feedback capacitor in this circuit. This is due to the fact that there is already about 1pF capacitance inherent in the 150K resistor.

The circuit was tested by connecting a 1pF capacitor to the input and applying a 1V voltage step to the other terminal of the capacitor. This was done to simulate the charge on the cathode. An oscillator trace of the output is displayed in figure 6.4. The output signal has a rise–time of roughly 1ns and a time–constant of 62ns and a peak output of $1.58V$. This represents a gain of 1.58×10^{12} V/Coul. With the space limitations and configuration of the connector pins on the chamber. It is necessary to place six such amplifiers on one small PC board. The effect of this was studied by prototyping four such circuits in close proximity on a copper ground plane. The result was that the cross–talk positive feedback between them led to oscillations. It may be possible, however, to eliminate this effect through the use of RF chokes on the power supplies

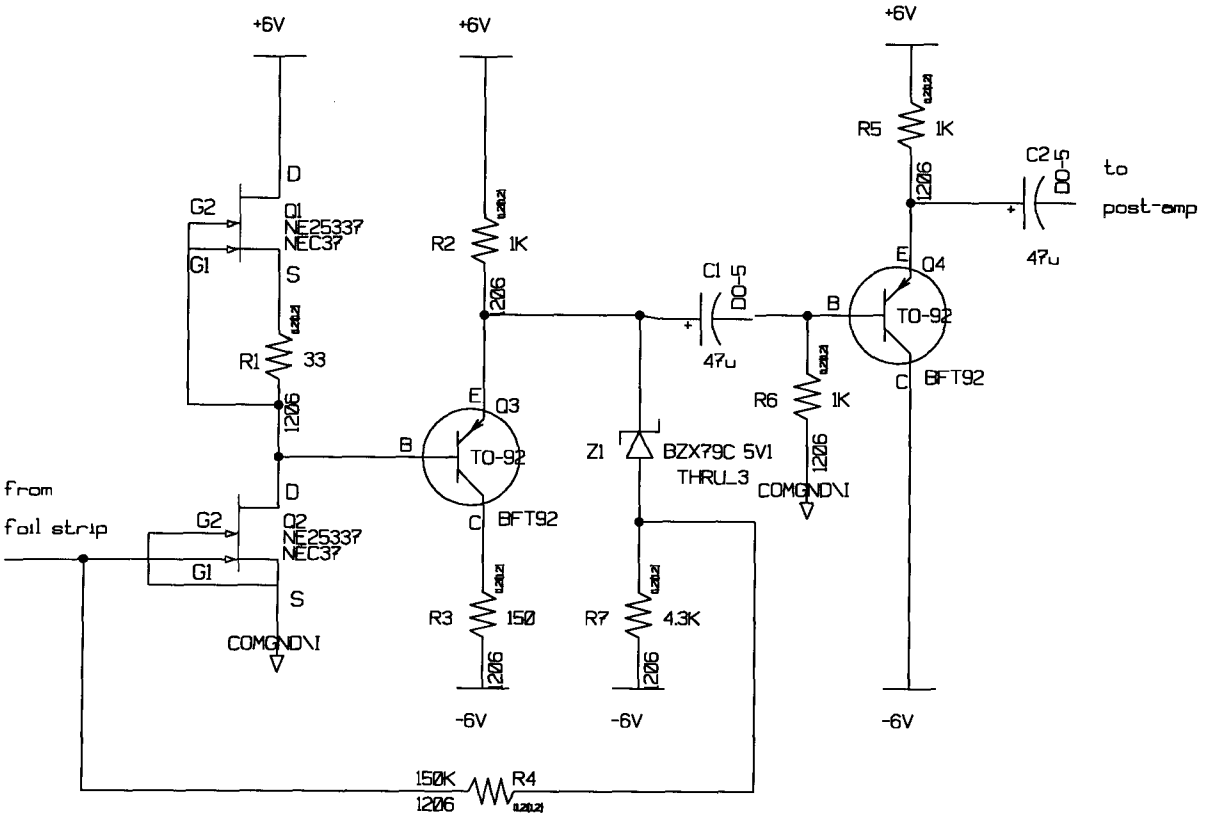

Figure 6.3: Circuit diagram for charge amplifier

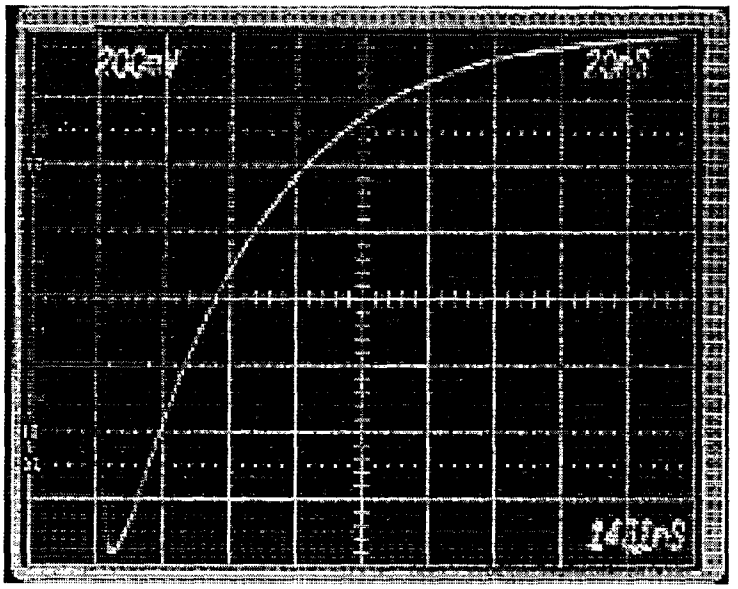

Figure 6.4: Scope trace of impulse response of charge amplifier

and by proper layout of the circuits.

Chapter 7

Conclusion

The UTC is a low–mass cylindrical drift chamber using signals on axial anode wires as well as helical cathode strips to measure the x,y, and z coordinates of charged particle tracks. It is intended to replace the present drift chamber in the E787 detector in order to improve the charged particle tracking and enhance the momentum resolution of the detector from 2% to 1%. The lower mass of the UTC is achieved through the use of zinc–gold plated aluminium cathode wires instead of Be–Cu wires, the use of cathode foil strips for z–position measurement rather than extra layers of stereo sense wires, the use of helium filled spacer regions, and through the use of plastic (Noryl) for the endplates and foil rings.

The time development of the signal on a cathode strip differs from that on an anode wire. Thus, while it is possible to use the pre–amplifiers that instrumented the stereo wires on the old drift chamber to read out the foil strips, these would not be optimal. Superior gain and signal–to–noise can be achieved with the use of a charge amplifier such as the one presented in chapter 6. Furthermore, capacitative coupling of the foil strips to the ground plane is causing attenuation of the signals on the inner two foils. Thus, improved signal gain from the pre–amplifiers would serve to remedy the situation. The alternative to this would be to to increase the field in the first superlayer and use the increased gas gain to compensate for the reduced signal on foils 1 and 2. The drawbacks to this would be spurious field emission and accelerated ageing of the chamber.

The desired gain has been achieved using one amplifier in isolation. However, when several are placed in close proximity on a single board problems with cross-talk leading to oscillation were observed. These problems are currently under study.

Bibliography

[1] M.S Attiya *et. al.* (The E787 Collaboration), *Phys. Rev. Lett.* **70** (1993) 2521

[2] J. Ellis, J. Hagelin, *Prog. Part. Nucl. Phys.* **23** (1983) 1

[3] S.L Glashow, J. Iliopoulos, and L. Maiani, *Phys. Rev.* **D2** (1970) 1285

[4] T.Inami, C.S Lim, *Prog. Theor. Phys.* **65** (1981) 297

[5] L.S Littenberg, E787 Technical Note 179 (18 October 1990, unpublished)

[6] J. Haggerty, E787 Technical Note 196, (6 November 1990, unpublished)

[7] L. Wolenstein, *Phys. Rev. Lett.* **51** (1983) 1945

[8] F. Abe. *et. al.* (The CDF Collaboration), FERMILAB-PUB-90-137-E (July 1990, unpublished)

[9] D. Akerib, D. Marlow, P. Meyers, E787 Technical Note 1986 (8 August 1990, unpublished)

[10] C.S Kim, J.L Rosner, C.-P. Yuan, *Phys. Rev.* **D42** (1990)

[11] M.S Attiya *et. al.* (The E787 Collaboration), *Nuclear Instruments and Methods in Physics Research* **A321** (1992) 129

[12] E. Blackmore, D.Bryman, Y. Kuno, P. Padley, T. Numao, E787 Technical Note 182 (12 February 1991, unpublished)

[13] Y. Kuno, E787 Technical Note 200 (23 January 1991, unpublished)

[14] R.A MacPherson, M.R Convery, M.M Ito, D.R Marlow, W.R Sands, E787 Technical Note 212 (7 August 1991, unpublished)

[15] A. Konaka, *private communication*

[16] F. Sauli, *Principles of Operation of Multiwire Drift and Proportional Chambers* CERN report 77-09, May 3, 1977

[17] D. Bryman, *International Journal of Modern Physics* **4** (1989) 79

[18] J.V Cresswell *et al.*, *IEEE Transactions on Nuclear Science* **35** (1988) 460

[19] Rob Veenhoff, *A drift chamber simulation program v2.02*, CERN (1990)

[20] P. Renton, Electroweak Interactions, Cambridge University Press, Cambridge, 1990, 596p.

[21] E. Segre, Nuclei and Particles, *2nd ed.*, W.A Benjamin Inc., Reading, Massachusets, 1977, 966p.

[22] V. Kujala, Master's Thesis, University of Victoria, 1991

[23] D.S Akerib, Ph.D Thesis, Princeton University, 1991

[24] W.C Louis, E787 Technical Note 150 (12 May 1988, unpublished)

[25] S.L Glashow, J.Illiopoulos, L. Maiani, *Phys. Rev.* **D2** (1970) 1285

[26] R.P Feynman, M. Gell–Mann, *Phys. Rev.* **109** (1958) 193

[27] N. Cabibbo, *Phys. Rev. Lett.* **10** (1963) 531

[28] J. Ellis, J.S Hagelin, *Nucl. Phys.* **B217** (1983) 189

[29] M.K Gaillard, Y.C Kao, I–H. Lee, M. Suzuki *Phys. Lett.* **123B** (1983) 241

[30] S. Bertolini, A. Masiero *Phys. Lett.* **49** (1986) 1549

[31] M. Kobayashi, T. Maskawa, *Prog. Theor. Phys.* **49** (1972) 282

[32] U. Turke, *Phys. Lett.* **168B** (1986) 296